

# QuickNAT: Segmenting MRI Neuroanatomy in 20 seconds

Abhijit Guha Roy, Sailesh Conjeti, Nassir Navab and Christian Wachinger

## Affiliations:

A. Guha Roy, C. Wachinger

Laboratory for Artificial Intelligence in Medical Imaging (AI-Med),  
Department of Child and Adolescent Psychiatry, Psychosomatic and  
Psychotherapy,  
Ludwig-Maximilian-University,  
Waltherstr. 23, 80337 Munich, Germany

A. Guha Roy, S. Conjeti, N. Navab

Chair for Computer Aided Medical Procedures, Department of Informatics  
Technical University of Munich,  
Boltzmannstr. 3, 85748 Garching, Munich, Germany.

S. Conjeti

German Center for Neurodegenerative Diseases (DZNE)  
Sigmund-Freud-Str. 27, 53127 Bonn, Germany.

N. Navab

Chair for Computer Aided Medical Procedures  
Johns Hopkins University,  
3400 North Charles Street, Hackerman 200,  
Baltimore, Maryland 21218, USA.

## **Abstract**

Whole brain segmentation from structural magnetic resonance imaging is a prerequisite for most morphological analyses, but requires hours of processing time and therefore delays the availability of image markers after scan acquisition. We introduce QuickNAT, a fully convolution neural network that segments a brain scan in 20 seconds. To enable training of the complex network with limited annotated data, we propose to pre-train on auxiliary labels created from existing segmentation software and to subsequently fine-tune on manual labels. In an extensive set of evaluations on eight datasets that cover a wide age range, pathology, and different scanners, we demonstrate that QuickNAT achieves superior performance to state-of-the-art methods, while being about 700 times faster. This drastic speed up greatly facilitates the processing of large data repositories and supports the translation of imaging biomarkers by making them almost instantaneously available.

Magnetic Resonance Imaging (MRI) provides detailed in-vivo insights about the morphology of the human brain, which is essential for studying development, aging, and disease (Alexander-Bloch and Giedd, 2013; Draganski et al., 2004; Giedd et al., 1999; Lerch et al., 2017; Raznahan et al., 2012; Shaw et al., 2006; Wachinger et al., 2016). In order to access measurements like the volume, thickness, or shape of a structure, the neuroanatomy needs to be segmented, which is a time-consuming process when performed manually (Fischl et al., 2002). Computational tools have been developed that can fully automatically segment brain MRI scans by warping a manually segmented atlas to the target scan (Ashburner and Friston, 2005; Fischl et al., 2002; Rohlfing et al., 2005; Svarer et al., 2005). Such approaches have two potential shortcomings: the estimation of the 3D deformation field for warping is computationally intense and the restriction to homologies may result in erroneous segmentations of the cortex (Lerch et al., 2017). Due to these drawbacks, existing atlas-based methods require hours of processing time for each scan and sometimes may result in sub-optimal solutions.

We propose a method for the Quick segmentation of NeuroAnaTomy (QuickNAT) in MRI scans based on a deep fully convolutional neural network (F-CNN) that runs in 20 seconds, compared to hours for existing atlas-based methods. We believe that this drastic speed up by several orders of magnitude will dramatically change our perception of image reconstruction and can therefore have a wide impact on neuroimaging. Not only will the processing of large datasets be possible with a single Graphics Processing Unit, instead of a computing cluster; it will also allow for almost instantaneous access to quantitative morphological measurements after the scan, boosting its translation in the clinical practice. In addition, QuickNAT produces segmentations of high accuracy for a wide age range, different field strengths, and in the presence of pathologies. Moreover, it yields effect sizes that are closer to those of manual segmentations and therefore offers advantages for group analyses. Finally, QuickNAT exhibits high test-retest accuracy making it useful for longitudinal studies.

Deep learning models have had ample success over last years, but require vast amounts of annotated data for effective training (LeCun et al., 2015). The limited amount of training data with manual annotations presents the main challenge in extending F-CNN models,

which have been proposed for semantic image segmentation in computer vision (Long et al., 2015), to brain segmentation. To address this challenge, we introduce a new training strategy (Fig. 1) that exploits large brain repositories without manual labels and small repositories with manual labels. In the first step, we apply existing software tools (e.g., FreeSurfer (Fischl et al., 2002)) to segment scans without annotations. We refer to these automatically generated segmentations as auxiliary labels, which we use to pre-train the network. Auxiliary labels may not be as accurate as expert annotations; however, they allow us to efficiently leverage the vast amount of initially unlabeled data for supervised training of the network. It also makes the network familiar with a wide range of morphological variations of different brain structures that may exist in a wide population. In the second step, we fine-tune (i.e., continue training) the previous network with the limited manually annotated data. The pre-training provides a good prior initialization of the network, so that the scarce manual annotations are optimally utilized to achieve high segmentation accuracy. QuickNAT is the first method that exploits the high testing speed of fully-convolutional networks for whole brain segmentation and uses unlabeled neuroimaging data with auxiliary labels for training them.

QuickNAT consists of three 2D F-CNNs operating on coronal, axial and sagittal views followed by a view aggregation step to infer the final segmentation (Fig. 2b, Methods). Each F-CNN has the same architecture and is inspired from the traditional encoder/decoder based U-Net architecture with skip connections (Ronneberger et al., 2015) enhanced with unpooling layers (Noh et al., 2015) (Fig. 2a). We also introduce dense connections (Huang et al., 2016) within each encoder/decoder blocks, to aid gradient flow and to promote feature re-usability, which is essential given the limited amount of training data. The network is optimized using a joint loss function of weighted logistic loss and multi-class Dice loss, where we compensate for high class imbalance in the data and encourage proper estimation of anatomical boundaries using an appropriate weighting scheme (Methods). The two main methodological innovations of QuickNAT are the training strategy with auxiliary labels and the F-CNN architecture. The code and trained model are available as extensions of MatConvNet (Vedaldi and Lenc, 2015) for off-the-shelf use.

## Results

We evaluate QuickNAT in a comprehensive series of eight experiments (details in Supplementary Experiments) to assess the accuracy, reproducibility and sensitivity on a large variety of neuroimaging datasets (description of datasets in Supplementary Datasets and Supplementary Table 1). In all experiments, we pre-train QuickNAT on 581 MRI volumes from the IXI dataset<sup>1</sup> processed with FreeSurfer (Fischl et al., 2002) to get auxiliary segmentations. The datasets used for pre-training, fine-tuning, and testing together with the purpose of each experiment are stated in Table 1. In experiments 1 to 5, we assess the segmentation accuracy, which requires datasets with manual annotations for the evaluation. In experiments 6 to 8, we assess the reliability and consistency of QuickNAT segmentations.

### Evaluation of segmentation accuracy

#### Training and testing on same dataset

In experiment 1, we work with 30 manually labeled scans from the multi-atlas labelling challenge (MALC) dataset (Landman and Warfield, 2012). Out of these, 15 scans are used for fine-tuning the network and the remaining 15 scans are used for testing, consistent with the original challenge setup. Fig. 3a and Supplementary Table 2 show the segmentation results of QuickNAT compared to (i) state-of-the-art F-CNN models U-Net (Ronneberger et al., 2015) and FCN (Long et al., 2015), (ii) state-of-the-art deep learning based whole-brain segmentation DeepNAT (Wachinger et al., 2017), (iii) Spatial STAPLE (Asman and Landman, 2012) (within Top 5 in MALC), and (iv) PICSL (Wang and Yushkevich, 2013) (winner of MALC). Spatial STAPLE and PICSL are atlas-based methods from the challenge, whose segmentation results were provided. The segmentation accuracy measured in Dice overlap ratio (Methods) shows the overall best results for QuickNAT (Supplementary Table 2). QuickNAT with pre-training yields significantly higher Dice scores than direct training on the manual segmentations. Also, the improvements over U-Net, FCN, and Spatial STAPLE are significant.

---

<sup>1</sup> <http://brain-development.org/ixi-dataset/>

In a structure-wise comparison (left hemisphere Fig. 3a, all structures Supplementary Fig. 1), there are no significant differences to the challenge winner PICSL, whereas QuickNAT has significantly higher Dice for many structures compared to Spatial STAPLE (14 of 27) and U-Net (23 of 27). Qualitative results confirm the good performance of QuickNAT compared to PICSL and the improvement when combining pre-training with fine-tuning (Fig. 3b). The runtime of QuickNAT is 20s per volume, which is orders of magnitudes faster than alternative atlas-based and deep learning based methods that take several hours (Fig. 3c). Running QuickNAT only on coronal slices leads to a slight drop in performance but reduces the runtime to about 6s. Volume distance results on test/retest data from five subjects, which were chosen by the challenge organizers, show a high inter-run consistency, comparable to atlas-based methods (Supplementary Table 3).

### **Training and testing on different datasets**

In the following experiments, we evaluate the generalizability of QuickNAT by deploying the network on datasets that have not been used for training. We increase the number of training scans from MALC from 15 to 28 and compare to FreeSurfer, which is the most frequently used tool for neuroanatomical reconstruction. Note that manual annotations of the training/testing dataset are done following the same protocol as the FreeSurfer atlas, defined by Center for Morphometric Analysis at Massachusetts General Hospital<sup>2</sup>. We assess the accuracy with respect to the age of subjects, the presence of disease (Alzheimer's disease, AD), and the magnetic field strength. Finally, we evaluate the sensitivity of automated segmentation in comparison to manual segmentation in group analyses.

In experiment 2, we test whole brain segmentation on 29 scans from the Alzheimer's Disease Neuroimaging Initiative (ADNI) that were manually annotated by Neomorphometrics Inc. ADNI (Jack et al., 2008) is one of the largest longitudinal neuroimaging studies to date and the segmentation is of high medical relevance. We report structure-wise Dice scores for the left hemisphere in Fig. 4 and for all structures in Supplementary Fig. 2 with significantly higher scores for QuickNAT than FreeSurfer in 24 out

---

<sup>2</sup> <http://www.cma.mgh.harvard.edu/manuals/segmentation/>

of 27 structures. ADNI-29 contains 15 controls and 14 AD patients, where we show the segmentation accuracy across each group in Fig. 5; the figure also reports results across field strengths (1.5T, 3.0T). QuickNAT produces significantly higher Dice scores for both groups and field strengths indicating its generalizability across these groups.

We further evaluate, whether the higher accuracy translates into advantages in the group analyses between controls and AD. First, we analyze effect sizes between the groups by computing Hedge's  $g$  and Glass'  $\Delta$  with their confidence margins (Methods) for the segmentations of hippocampus and amygdala with QuickNAT and FreeSurfer as well as the manual segmentation. Effect sizes of QuickNAT are closer to the ones from the manual segmentation than FreeSurfer (Table 2). Second, we compute  $p$ -values for the association between diagnosis and volume with age and sex as covariates. All segmentations show significant associations for hippocampus and amygdala, however, the  $p$ -values obtained from volume estimates with QuickNAT are more similar to the ones from the manual segmentation (Supplementary Table 5).

In experiment 3, we test on 18 T1 MRI scans with manual whole brain segmentations from the Internet Brain Segmentation Repository (IBSR). Challenges of this dataset include lower resolution of 1.5mm in anterior-posterior direction (high slice thickness), low contrast and a wide age range from 7 to 71 years. Results on IBSR show a higher Dice score for QuickNAT than for FreeSurfer (structure-wise results for left hemisphere in Fig. 6, both hemispheres in Supplementary Fig 3, and mean Dice scores in Supplementary Table 7). For 16 out of 27 structures, the improvements are statistically significant.

In experiment 4, we test whole brain segmentation on 13 T1 MRI brain scans from the Child and Adolescent NeuroDevelopment Initiative (CANDI) (Kennedy et al., 2012) that were manually annotated by Neomorphometrics Inc. The dataset includes scans from children and adolescents from 5 to 15 years of age, some of them with psychiatric disorders. The aim of the experiment is to investigate the robustness of QuickNAT for the segmentation of scans from such a young age range, where a challenge is that scans from that age range were not used for training. We plot Dice scores per structure in Fig. 7 (left hemisphere) and

Supplementary Fig. 4 (whole brain), together with the average Dice score in Supplementary Table 8. With an average Dice score of 0.84, we obtain very good segmentation results on CANDI. This is confirmed in a comparison to FreeSurfer, which is outperformed by a statistically significant in 22 out of 27 structures.

In experiment 5, we evaluate the hippocampus segmentation in the presence of dementia on a large dataset with manual annotations following the Harmonized Protocol (HarP) for hippocampus segmentation (Boccardi et al., 2015), developed by the European Alzheimer's Disease Consortium and ADNI. Left and right hippocampi were segmented for 131 subjects, balanced for controls, mild cognitive impairment (MCI) and AD. Across all diagnostic groups (42 CN, 44 MCI, 45 AD), the volume distance to the manual segmentation is significantly lower for QuickNAT than FreeSurfer and the Dice scores are significantly higher (Fig. 8a, Supplementary Table 10). Processing the HarP dataset with FreeSurfer took about 540 hours, while QuickNAT only took 0.8 hours.

**Comparison to FSL FIRST:** As a final comparison of segmentation accuracy, we compare to FSL FIRST, which is another publicly available tool for automated segmentation of some sub-cortical structures for T1 MRI scans (Jenkinson et al., 2012; Patenaude et al., 2011). We cannot directly compare our results to FSL as it only segments 15 structures in the brain, whereas QuickNAT segments 27 structures. For a fair comparison, we selected the common 13 structures which are segmented by FSL, QuickNAT and FreeSurfer (thalamus, caudate, pallidum, hippocampus, amygdala, brainstem) and present results on ADNI-29, CANDI, and IBSR in Supplementary Table 9. We noted that FSL failed on several scans IBSR (44%) than on ADNI (17%) or CANDI (23%), whereas FreeSurfer and QuickNAT have not produced any failures. Identical to FreeSurfer, FSL was run with recommended default settings. Considering all scans, QuickNAT outperforms both FreeSurfer and FSL by a statistically significant margin ( $p < 0.001$ ). Excluding the scans where FSL failed, QuickNAT demonstrates superior performance for ADNI-29, while FSL is best for CANDI. A possible reason for the good performance of FSL on CANDI may be that FSL includes scans with age range (5-15 years) in its atlas.



## Evaluation of segmentation reliability

In experiment 6, we follow a comprehensive testing protocol for MRI neuroanatomical segmentation techniques as proposed for lateral ventricle segmentation, termed ALVIN (Kempton et al., 2011). The dataset consists of 7 young adults and 9 patients with Alzheimer’s disease. Lateral ventricles have been manually annotated at two time points to observe intra-observer variability and the volumes were reported. We compute the volumes from QuickNAT segmentations and follow the evaluation protocol by reporting intra-class correlation coefficient (ICC) (Kempton et al., 2011), in addition to volume distance (Methods). We compare to results of FreeSurfer and ALVIN reported in (Kempton et al., 2011). On control subjects, QuickNAT shows the best results for the first annotation and the second-best results for the second annotation (Fig. 8b, Supplementary Table 11). On AD patients, QuickNAT resulted in the best performance.

In experiment 7, we conducted a reliability study on Test-Retest (TRT) dataset (Maclaren et al., 2014). The data includes 120 MRI T1 scans for 3 subjects (40 scans/subject), over 20 sessions (2 scans/session) acquired within a period of 31 days. We analyzed the same set of 8 structures selected by (Maclaren et al., 2014) and also measure the coefficient of variation (CV) (Methods). Table 3 (A) reports the inter-session variation for QuickNAT and FreeSurfer, where Supplementary Table 12 also states the intra-session variation. Inter-session variation is lower for QuickNAT than FreeSurfer on 7 out of 8 structures. Only for cerebral white matter FreeSurfer was more consistent, possibly due to the sophisticated surface processing and correction stage that follows the initial segmentation (Dale et al., 1999; Fischl et al., 1999).

In experiment 8, we evaluated the reliability in estimating volumes across scans acquired from multiple centers, from the Human Travelling Phantom (HTP) dataset (Magnotta et al., 2012). The dataset consists of MRI T1 scans from 5 healthy subjects scanned in 8 different sites in the USA. All scans were acquired within a period of 30 days. The identical structures to experiment 7 were selected for analysis. The coefficient of variation (CV) is computed

across centers for each subject, and summarized in the root-mean-square (RMS) CV per structure (Methods). Table 3 (B) reports the RMS CV for QuickNAT and FreeSurfer, with more detailed results per subject in Supplementary Table 13. QuickNAT is more consistent than FreeSurfer for 4 out of 8 structures, indicating similar robustness to FreeSurfer across multiple centers.

## Discussion

We have introduced QuickNAT, a deep learning based method for brain segmentation that runs in 20 seconds, achieving superior performance with respect to existing methods and being orders of magnitudes faster. We have demonstrated that the method generalizes well to other, unseen datasets (training data different to testing) and yields high segmentation accuracy across diagnostic groups, scanner field strengths, and age, while producing highly consistent results. This high segmentation accuracy enhances group analyses by enabling effect sizes and significance values that better match those of manual segmentations. Also, with high test-retest accuracy it can be effectively used for longitudinal studies. QuickNAT can have a dramatic impact on clinical practice, because of its fast processing time and robustness to neuroanatomical variability, allowing for an almost instantaneous and accurate access to imaging biomarkers.

Although, deep learning models are proven to be highly effective, they are highly complex and require a lot of annotated data for effective training (LeCun et al., 2015). Access to such abundant annotated training data is often restricted for medical applications due to the high cost of creating such annotations. The problem is more prominent for F-CNNs, where each slice corresponds to one data point, in contrast to patch based approaches, where millions of patches can be extracted from a volume (Wachinger et al., 2017). To address this issue, we introduced a training strategy that leverages the surplus unlabeled data and the limited manual data to effectively train our fully convolutional model. We used FreeSurfer to create automatic segmentations on the unlabeled data, which serve as auxiliary labels to pre-train the model. This pre-trained model, which mimics FreeSurfer, is fine-tuned with limited manually annotated data to get the final model. Our results have shown that the model trained with this new strategy significantly outperforms the model that is only trained on manual data. Although we have demonstrated the application to brain segmentation, the proposed training strategy is generic and can be effectively used for other segmentation tasks as well.

The architecture of QuickNAT is custom-made for addressing the challenges associated with whole brain segmentation. The fully convolutional architecture offers faster processing and larger context than patch-based DeepNAT (Wachinger et al., 2017), because all the voxels in

a slice are labelled simultaneously. The dense connections within every encoder and decoder block promote feature re-usability in the network (Huang et al., 2016), which optimizes model complexity by avoiding learning of similar feature maps in different layers. In the decoder blocks, upsampling is done using unpooling layers instead of convolutions, which not only doesn't involve any learnable parameters but also enforces spatial consistency; an essential aspect for segmenting small sub-cortical structures. The network is learnt by optimizing a combined weighted logistic and Dice loss function with stochastic gradient descent. Weighting is done to highlight under-represented classes using median frequency balancing and anatomical boundaries, thus to tackle class imbalance and provide reliable contour estimation of the structures. Our results have shown the significant improvement of the QuickNAT architecture, compared to state-of-the-art U-Net and FCN models.

We have demonstrated the high accuracy of QuickNAT on a comprehensive set of 5 experiments that cover a wide range of variations in acquisition parameters and neuroanatomy. In experiments on the MALC dataset, we demonstrated that QuickNAT provides segmentations with similar accuracy and inter-run consistency to the best atlas-based methods, while being orders of magnitude faster (Fig. 3). In experiments with ADNI-29, we demonstrated the robustness of QuickNAT with respect to pathology (Fig. 4a) and magnetic field strengths (Fig. 4b). Moreover, effect sizes from QuickNAT are more similar to those from manual segmentations than FreeSurfer (Table 2). In experiments with IBSR, we demonstrated the robustness to data with lower resolution and low contrast (Fig. 5). The high segmentation accuracy on scans from young subjects was presented on the CANDI dataset (Fig. 6) and for the hippocampus segmentation on the HarP dataset (Fig. 7). Finally, we compared to FSL FIRST on a subset of structures that are identified by both. Noteworthy, QuickNAT has not failed on any scan across all datasets and has not produced a single segmentation that had to be entirely rejected.

In an additional set of 3 experiments, we evaluated the reliability of QuickNAT. We measured high reliability in lateral ventricle segmentation by following the testing protocol ALVIN. We observed high consistency for the segmentation of 8 structures on test-retest data with less than 2% variation on most brain structures (Table 3). The test-retest data was acquired on the same scanner. We extended the evaluation to a more challenging dataset,

where the same subject was scanned in various machines at different sites. As expected, the variation increased in this setup, but the reliability was comparable to FreeSurfer. The high reliability of QuickNAT compared to FreeSurfer is surprising, because the atlas used in FreeSurfer provides a strong spatial prior, which tends to improve reliability. However, our results showed that the more unconstrained, deep learning based segmentation can achieve higher reliability.

QuickNAT is about 700 times faster than currently used software for whole-brain segmentation, which can widely impact neuroimaging. We are currently seeing a massive increase in neuroimaging datasets, many containing over 10,000 scans (Bamberg et al., 2015; Breteler et al., 2014; Jack et al., 2008; Miller et al., 2016). Such huge datasets are collected to study complex problems, e.g., associations between imaging and genetics. QuickNAT allows for processing such large repositories on a single GPU workstation in a reasonable amount of time, without the need for accessing large computing clusters. Furthermore, years of research in neuroimaging have identified a wide range of imaging biomarkers for neurodegenerative and psychiatric disorders (Abi-Dargham and Horga, 2016; Jack et al., 2013, 2008). However, the translation of such markers to the daily diagnostic routine is still lacking. Processing times of several hours by current methods, which cannot be substantially reduced on computing clusters as parallelization mainly happens at the scan level, may be one obstacle. We believe that the almost instantaneous access to imaging biomarkers provided by QuickNAT can therefore boost the translation to the clinic.

As any brain segmentation method, QuickNAT has limitations. On the data of the human traveling phantom, we observed an increase in variance across centers. In a detailed investigation, we found that scans from one of the sites (Dartmouth) had strong motion artifacts, which deteriorated our segmentation performance, and in turn increased the variation. Motion artifacts present a challenge to many image processing tasks. If more than one source volume exists, motion correction could be applied, as it is for instance done in the FreeSurfer pipeline. Another limitation of QuickNAT is that it cannot deal with a tissue classes that are not part of the training set, e.g., tumors. For QuickNAT to also work on tumor cases, we would need training data, where the tumor is annotated together with all the brain structures. To the best of our knowledge, such a dataset is not publicly available.

In spite of the limitations, we believe that QuickNAT will have a high impact in neuroimaging as it provides highly accurate segmentations for scans from a wide age range, with pathology, and acquired with different scanners, while only requiring 20 seconds of processing time.

## Methods

### Architecture Design

QuickNAT has an encoder/decoder like F-CNN architecture with 4 encoders, 4 decoders separated by a bottleneck layer (Fig. 2a). This is followed by a classifier block with a soft-max layer. The architecture includes skip connections between all encoder and decoder blocks of the same spatial resolution, similar to the U-Net architecture (Ronneberger et al., 2015). These skip connections not only provide high contextual information to the decoders, but also provide a path of gradient flow from the shallower layers to deeper layers, improving the training. In the decoder stages, instead of up-sampling the feature maps by convolution transpose like U-Net, we included un-pooling layers (Noh et al., 2015). These ensure appropriate spatial mappings of the activation maps during up-sampling, which in turn helps in accurate segmentation especially for small sub-cortical structures.

**Dense Block:** Each dense block consists of three convolutional layers (Fig. 2a). Every convolutional layer is preceded by a batch-normalization layer and a Rectifier Linear Unit (ReLU) layer. The first two convolutional layers are followed by a concatenation layer that concatenates the input feature map with outputs of the current and previous convolutional blocks. These connections are referred to as dense connections (Huang et al., 2016) and provide a path for gradients to flow for better trainability and promote feature re-usability across different stages of convolution (Huang et al., 2016). In addition, they help better representation learning by preventing similar features being learnt in different convolution layers within the block. The kernel size for these two convolutional layers is kept small (5x5) to limit the number of parameters. Appropriate padding is provided so that the size of feature maps before and after convolution remains the same. The output channels for each convolution layer is set to 64, which acts as a bottleneck for feature map selectivity. The input channel size is variable, depending on the number of dense connections. The third convolutional layer is also preceded by a batch normalization and ReLU but has a 1x1 kernel size to compress the feature map size to 64. A flow diagram of the dense block is illustrated in Fig. 2a.

**Encoder Path:** The encoder path consists of a set of 4 dense blocks, each followed by a 2x2 max-pooling block, which reduces the spatial dimension of the feature maps by half at each stage. During down-sampling by max-pooling, the indices corresponding to the maximum activations are saved and passed to decoder blocks for un-pooling.

**Bottleneck Block:** The bottleneck block consists of a 5x5 convolutional layer and a batch normalization layer to separate the encoder and decoder part of the network, providing a bottleneck in information passing between the encoder and decoder.

**Decoder Path:** The decoder path also consists of 4 dense blocks. Each dense block is preceded by an un-pooling layer, which up-samples by mapping the input feature map, using the indices from the corresponding max pooling layer of the encoder path. This layer recovers the actual spatial locations corresponding to the maximum activations, which are lost during max-pooling in the encoders, and places them at the correct location during up-sampling (Noh et al., 2015). This is very relevant for the segmentation of small sub-cortical structures. A further advantage of up-sampling is that it doesn't involve any learnable parameters in comparison to convolutional transpose used in U-Net (Ronneberger et al., 2015). The up-sampling is followed by a skip-connection, which concatenates the un-pooled feature map with the output feature map of the corresponding encoder before max-pooling. Skip connections add high contextual information for segmentation and allow gradients to flow from shallower to deeper regions of the network. The concatenated block is passed to the dense block with similar architecture.

**Classifier Block:** The output feature map from the last decoder block is passed to the classifier block which is basically a convolutional layer with 1x1 kernel size that maps the input to an  $N$  channel feature map, where  $N$  is the number of class (28 in our case). This is followed by a soft-max layer to map the activations to probabilities, so that all the channels represent probability maps for each of the classes.

### Loss Function

QuickNAT is learnt by optimizing two loss functions simultaneously, (i) weighted logistic loss and (ii) multi-class Dice loss. The logistic loss provides a pixel-wise probabilistic estimate of similarity between the estimated labels and the ground truth. The Dice loss is inspired from the Dice overlap ratio, which estimates similarity between the estimated and ground truth labels (Milletari et al., 2016). It was initially introduced for two-class segmentation and



extended to multi-class segmentation in this work in combination with logistic loss. Given the probability of class  $l$  at pixel  $\mathbf{x}$  by  $p_l(\mathbf{x})$  and the ground-truth by  $g_l(\mathbf{x})$ , the loss function is

$$L = \underbrace{-\sum_{\mathbf{x}} w(\mathbf{x})g_l(\mathbf{x}) \log(p_l(\mathbf{x}))}_{\text{Logistic Loss}} - \underbrace{\frac{2 \sum_{\mathbf{x}} p_l(\mathbf{x}) g_l(\mathbf{x})}{\sum_{\mathbf{x}} p_l^2(\mathbf{x}) + \sum_{\mathbf{x}} g_l^2(\mathbf{x})}}_{\text{Dice Loss}}. \quad (1)$$

The first term is the multi-class logistic loss and the second term is the Dice loss. We introduce a weighting term  $w(\mathbf{x})$ , which balances the relative importance of pixels for the loss computation. We set the weight to address two challenges: (i) the class imbalance and (ii) errors in segmentations at the anatomical boundaries. Given the frequency of class  $l$  by  $f_l$  in the training set, the indicator function  $I$ , the training segmentation  $S$ , and the 2D gradient operation  $\nabla$ , the weights are computed as

$$w(\mathbf{x}) = \sum_l I(S(\mathbf{x}) == l) \frac{\text{median}(\mathbf{f})}{f_l} + w_0 I(|\nabla S(\mathbf{x})| > 0), \quad (2)$$

where  $\mathbf{f} = [f_1, f_2, \dots, f_N]$  is the vector of all class frequencies. The first term models the median frequency balancing (Badrinarayanan et al., 2015), which compensates for the class imbalance by boosting the gradients from the classes with low probability, similar to instance re-sampling. The second term penalizes the error at anatomical boundaries.  $w_0$  balances the two terms and is set to  $w_0 = \frac{2 \text{median}(\mathbf{f})}{f_{\min}}$  to give higher priority to boundaries.

## Model Learning

We train QuickNAT with stochastic gradient descent with momentum. The learning rate is initially set to 0.1 and reduced by one order after every 10 epochs during pre-training. The weight decay term is set to 0.0001. Batch size is set to 4 limited by the 12GB RAM of the NVIDIA TITAN X Pascal GPU. The momentum is set to a high value of 0.95 to compensate for the noisy gradients due to small batch size.

## Training with Limited Annotated Data

F-CNN models directly produce a segmentation for all image pixels in an end-to-end fashion without the need of splitting the image into patches. They can therefore fully exploit the

image context avoiding artificial partitioning of an image, which also results in an enormous speed-up. Yet, training F-CNNs is challenging because each image serves as a single training sample and consequently much larger datasets with manual labels are required than for patch-based approaches, where each image provides many patches. While the amount of unlabeled data rapidly grows, the access to labeled data is still limited due to the labor intense process of manual annotations. At the same time, the success of deep learning is mainly driven by supervised learning, while unsupervised approaches are still an active field of research. Data augmentation artificially increases the training dataset by simulating different variations of the same data, but it cannot encompass all possible population level anatomical variations. We propose to process unlabeled data with existing software tools to create auxiliary labels. These auxiliary labels are not optimal; however, they allow us to use the vast amount of initially unlabeled data for supervised pre-training of the network, enforcing a strong prior. The training procedure consists of two main steps (Fig. 1):

- 1. Pre-training on large unlabeled datasets with auxiliary labels:** In this step, we use a large neuroimaging dataset (IXI dataset: <http://brain-development.org/ixi-dataset/>) and process it with an existing tool to create auxiliary labels. We apply the widely used FreeSurfer (Fischl et al., 2002) to obtain auxiliary segmentations, but also other tools could be used dependent on the application. We pre-train QuickNAT on this large dataset with auxiliary labels, which results in a network that imitates FreeSurfer segmentations. Pre-training enforces a strong prior on the network, where robustness to data heterogeneity is encouraged by the diversity of the IXI dataset acquired from three centers with high age range, encompassing substantial anatomical variability.
- 2. Fine-tuning with limited manually labelled data:** In this step, we take the pre-trained model and fine-tune it with limited data having manual annotations. Instead of learning all filters from scratch, fine-tuning only focuses on rectifying discrepancies between auxiliary and manual labels. We use data from the Multi-Atlas Labelling Challenge dataset (Landman and Warfield, 2012) for fine-tuning. During this, we lower the initial learning rate to 0.01 and reduce it by an order after every 5 epochs until convergence.

## Multi-View Aggregation

To further include information from the third dimension to the 2D F-CNN, we train a separate network for each of the three principle views: coronal, axial and sagittal (Fig. 2b). The predictions for each these networks are combined to the final segmentation in a multi-view aggregation step. The final label for a voxel  $\mathbf{x}$  is given by  $L_{Pred}(\mathbf{x})$ , which is computed as

$$L_{Pred}(\mathbf{x}) = \mathbf{arg\ max}_c [\omega_1 \mathbf{p}_{AX}(\mathbf{x}) + \omega_2 \mathbf{p}_{COR}(\mathbf{x}) + \omega_3 \mathbf{p}_{SAG}(\mathbf{x})], \quad (3)$$

where  $\mathbf{p}_{AX}(\mathbf{x})$ ,  $\mathbf{p}_{COR}(\mathbf{x})$ ,  $\mathbf{p}_{SAG}(\mathbf{x})$  are the predicted probability vectors for axial, coronal and sagittal views and  $\omega_1, \omega_2, \omega_3$  the corresponding weights. The probability score for a particular structure reflects the certainty of the network in the prediction, which depends on how well the structure is represented in the corresponding view. Aggregating all the votes for a voxel provides a regularization effect for the label prediction and reduces spurious predictions.

The highly symmetric layout of the brain poses challenges for segmentation in sagittal slices, as it is not possible to differentiate slices from the left and right hemisphere. Thus, we assign structures from the left and right hemisphere the same label number for training on sagittal slices. This reduces the number of classes from 28 to 16. At testing, we re-map the probability maps from 16 to 28 structures by replicating probabilities for left and right. Due to this, we assign a lower value to  $\omega_3$  in comparison to  $\omega_1$  and  $\omega_2$ . In our case, we assign  $\omega_1, \omega_2, \omega_3$  to 0.4, 0.4 and 0.2 respectively.

## Evaluation metrics

Performance of QuickNAT is evaluated with the following metrics.

**Volume distance:** This metric indicates the error in volume estimation after segmentation. It is defined as

$$d_V(V_{GT}, V_{EST}) = \frac{2 \text{abs}(V_{GT} - V_{EST})}{(V_{GT} + V_{EST})},$$

where  $V_{GT}$  and  $V_{EST}$  are the ground truth volume (estimated from manual segmentation) and the estimated volume, respectively, for a given structure. Higher volume distance indicates poor estimation of volume and therefore an indirect measure of low segmentation quality.

**Dice overlap ratio:** This metric is used to evaluate the quality of segmentation based on the amount of overlap between ground truth and segmented output. It is estimated as

$$Dice = \frac{2 TP}{2 TP + FP + FN},$$

where  $TP$ ,  $FP$  and  $FN$  are the counts for true positives, false positives and false negatives, respectively. It ranges between [0,1], where higher Dice score indicates better segmentation performance.

**Inter-class correlation:** This metric indicates how closely related two groups of estimations are and computes as

$$ICC = \frac{1}{N s^2} \sum_{i=1}^N (X_i - \mu) (Y_i - \mu),$$

where  $\mathbf{X} = \{X_i\}$  and  $\mathbf{Y} = \{Y_i\}$  are the two groups with  $N$  samples each, with joint mean  $\mu$  and variance  $s^2$ . It ranges from [0,1] where 0 indicates no relation between the groups and 1 indicates absolutely similar groups.

**Glass'  $\Delta$ :** This is a metric indicating effect size between two populations. It is estimated as

$$\Delta = \frac{\mu_X - \mu_Y}{S_Y},$$

where  $\mu_X$  and  $\mu_Y$  are the means for the two populations  $X$  and  $Y$ , respectively, and  $S_Y$  is the standard deviation for the population  $Y$ , which is taken as control population. This metric is unbounded and higher absolute value corresponds to a larger difference between the groups.

**Hedges'  $g$**  : This metric indicates the effect size and is estimated as

$$g = \frac{\mu_X - \mu_Y}{S^*} \left( \frac{N - 3}{N - 2.5} \right) \sqrt{\frac{N - 2}{N}},$$

where  $\mu_X$  and  $\mu_Y$  are the means for the two populations  $X$  and  $Y$ , respectively, and  $S^*$  is the pooled standard deviation for both the population. We use a variant of  $g$ , estimated by multiplying it with a constant (as shown above) as our sample size ( $N$ ) is less than 50. This is also interpreted similar to Glass'  $\Delta$ .

**Coefficient of Variation of volume estimate:** This metric provides a percentage variance measures in the different estimations. Lower the coefficient, better the estimator. The total coefficient of variation is computed as

$$CV_t = \frac{\sigma_t}{\mu_t} \times 100$$

where  $\sigma_t$  and  $\mu_t$  are the standard deviation and mean of the estimates (Maclaren et al., 2014). This global variance considering all the estimates across session provides inter-session  $CV_t$ . The intra-session co-efficient of variation  $CV_s$  is estimated by the root mean square of all the co-efficient of variance per session. In Table 3B of experiment 8, we report RMS CV, which is the root mean square of CV estimates for all the 5 patients.

**Wilcoxon rank-sum test:** This two-sided non-parametric statistical significance test is used in all of our experiments.

## **Implementation**

QuickNAT was implemented in Matlab R2016a, using the deep learning toolbox MatConvNet (beta 24) (Vedaldi and Lenc, 2015). All the processing and training was performed on a workstation with Intel Core i7-6850K 3.6Ghz, 128 GB of DDR4 PC2400 RAM, 1TB SSD, and two 12 GB NVIDIA TITAN X Pascal GPU running a 64-bit linux-based operating system. Pre-training took around 72 hours and fine-tuning 4 hours. We used FreeSurfer version 5.3 for all our experiments and have not performed any quality control or manual refinements. We used FSL FIRST release 5.0 in our experiments with default settings as recommended in the instruction manual. All training and testing data were pre-processed to bring to a standard orientation and isotropic resolution of 1mm, using the FreeSurfer routine `mri_convert`.

## **Code and model availability**

Code and trained model are available as Supplementary Software and online. They are also publicly available at: <https://github.com/abhi4ssj/QuickNATv2>. A runfile code is provided, which takes in MRI data as input and segments it, making the tool easy to use. Usage of the code needs the installation of CUDA libraries and availability of a GPU, which we believe will likely become the standard in the future. An integration into FreeSurfer is planned.

## **Data availability**

All MRI datasets analyzed during the current study are publicly available to ensure reproducibility with details described in Supplementary Table 1. The manual segmentations for MALC, IBSR, HarP and ALVIN datasets are also publicly available. The manual segmentations for ADNI-29 and CANDI are available from Neuromorphometrics Inc. but restrictions apply to the availability of these data, which were used under license for the current study.

## **Acknowledgment**

We are grateful to Neomorphometrics Inc. for providing manual segmentations of brain MRI scans. Support for this research was provided in part by the Bavarian State Ministry of Education, Science and the Arts in the framework of the Centre Digitisation.Bavaria (ZD.B) and by an NVIDIA hardware grant.

## References

- Abi-Dargham, A., Horga, G., 2016. The search for imaging biomarkers in psychiatric disorders. *Nat. Med.* 22, 1248–1255.
- Alexander-Bloch, A., Giedd, J.N., 2013. Imaging structural co-variance between human brain regions. *Nat. Rev. Neurosci.* 14, 322.
- Ashburner, J., Friston, K.J., 2005. Unified segmentation. *Neuroimage* 26, 839–851.
- Asman, A.J., Landman, B.A., 2012. Formulating spatially varying performance in the statistical fusion framework. *IEEE Trans. Med. Imaging* 31, 1326–1336.
- Badrinarayanan, V., Kendall, A., Cipolla, R., 2015. Segnet: A deep convolutional encoder-decoder architecture for image segmentation. *ArXiv Prepr. ArXiv151100561*.
- Bamberg, F., Kauczor, H.-U., Weckbach, S., Schlett, C.L., Forsting, M., Ladd, S.C., Greiser, K.H., Weber, M.-A., Schulz-Menger, J., Niendorf, T., 2015. Whole-body MR imaging in the German National Cohort: rationale, design, and technical background. *Radiology* 277, 206–220.
- Boccardi, M., Bocchetta, M., Morency, F.C., Collins, D.L., Nishikawa, M., Ganzola, R., Grothe, M.J., Wolf, D., Redolfi, A., Pievani, M., 2015. Training labels for hippocampal segmentation based on the EADC-ADNI harmonized hippocampal protocol. *Alzheimers Dement.* 11, 175–183.
- Breteler, M.M., Stöcker, T., Pracht, E., Brenner, D., Stirnberg, R., 2014. MRI IN THE RHINELAND STUDY: A NOVEL PROTOCOL FOR POPULATION NEUROIMAGING. *Alzheimers Dement. J. Alzheimers Assoc.* 10, P92.
- Dale, A.M., Fischl, B., Sereno, M.I., 1999. Cortical surface-based analysis: I. Segmentation and surface reconstruction. *Neuroimage* 9, 179–194.
- Draganski, B., Gaser, C., Busch, V., Schuierer, G., Bogdahn, U., May, A., 2004. Neuroplasticity: changes in grey matter induced by training. *Nature* 427, 311–312.
- Fischl, B., Salat, D.H., Busa, E., Albert, M., Dieterich, M., Haselgrove, C., Van Der Kouwe, A., Killiany, R., Kennedy, D., Klaveness, S., 2002. Whole brain segmentation: automated labeling of neuroanatomical structures in the human brain. *Neuron* 33, 341–355.
- Fischl, B., Sereno, M.I., Dale, A.M., 1999. Cortical surface-based analysis: II: inflation, flattening, and a surface-based coordinate system. *Neuroimage* 9, 195–207.
- Giedd, J.N., Blumenthal, J., Jeffries, N.O., Castellanos, F.X., Liu, H., Zijdenbos, A., Paus, T., Evans, A.C., Rapoport, J.L., 1999. Brain development during childhood and adolescence: a longitudinal MRI study. *Nat. Neurosci.* 2, 861–863.
- Huang, G., Liu, Z., Weinberger, K.Q., van der Maaten, L., 2016. Densely connected convolutional networks. *ArXiv Prepr. ArXiv160806993*.
- Jack, C.R., Bernstein, M.A., Fox, N.C., Thompson, P., Alexander, G., Harvey, D., Borowski, B., Britson, P.J., L Whitwell, J., Ward, C., 2008. The Alzheimer’s disease neuroimaging initiative (ADNI): MRI methods. *J. Magn. Reson. Imaging* 27, 685–691.
- Jack, C.R., Knopman, D.S., Jagust, W.J., Petersen, R.C., Weiner, M.W., Aisen, P.S., Shaw, L.M., Vemuri, P., Wiste, H.J., Weigand, S.D., 2013. Tracking pathophysiological processes in Alzheimer’s disease: an updated hypothetical model of dynamic biomarkers. *Lancet Neurol.* 12, 207–216.
- Jenkinson, M., Beckmann, C.F., Behrens, T.E., Woolrich, M.W., Smith, S.M., 2012. Fsl. *Neuroimage* 62, 782–790.
- Kempton, M.J., Underwood, T.S., Brunton, S., Stylios, F., Schmechtig, A., Ettinger, U., Smith, M.S., Lovestone, S., Crum, W.R., Frangou, S., 2011. A comprehensive testing protocol



- for MRI neuroanatomical segmentation techniques: evaluation of a novel lateral ventricle segmentation method. *Neuroimage* 58, 1051–1059.
- Kennedy, D.N., Haselgrove, C., Hodge, S.M., Rane, P.S., Makris, N., Frazier, J.A., 2012. CANDIShare: a resource for pediatric neuroimaging data. Springer.
- Landman, B., Warfield, S., 2012. MICCAI 2012 workshop on multi-atlas labeling, in: *Medical Image Computing and Computer Assisted Intervention Conference*.
- LeCun, Y., Bengio, Y., Hinton, G., 2015. Deep learning. *Nature* 521, 436–444.
- Lerch, J.P., van der Kouwe, A.J., Raznahan, A., Paus, T., Johansen-Berg, H., Miller, K.L., Smith, S.M., Fischl, B., Sotiropoulos, S.N., 2017. Studying neuroanatomy using MRI. *Nat. Neurosci.* 20, 314–326.
- Long, J., Shelhamer, E., Darrell, T., 2015. Fully convolutional networks for semantic segmentation, in: *Proceedings of the IEEE Conference on Computer Vision and Pattern Recognition*. pp. 3431–3440.
- Maclaren, J., Han, Z., Vos, S.B., Fischbein, N., Bammer, R., 2014. Reliability of brain volume measurements: A test-retest dataset. *Sci. Data* 1, 140037.
- Magnotta, V.A., Matsui, J.T., Liu, D., Johnson, H.J., Long, J.D., Bolster Jr, B.D., Mueller, B.A., Lim, K., Mori, S., Helmer, K.G., 2012. Multicenter reliability of diffusion tensor imaging. *Brain Connect.* 2, 345–355.
- Miller, K.L., Alfaro-Almagro, F., Bangerter, N.K., Thomas, D.L., Yacoub, E., Xu, J., Bartsch, A.J., Jbabdi, S., Sotiropoulos, S.N., Andersson, J.L., 2016. Multimodal population brain imaging in the UK Biobank prospective epidemiological study. *Nat. Neurosci.* 19, 1523–1536.
- Milletari, F., Navab, N., Ahmadi, S.-A., 2016. V-net: Fully convolutional neural networks for volumetric medical image segmentation, in: *3D Vision (3DV), 2016 Fourth International Conference On. IEEE*, pp. 565–571.
- Noh, H., Hong, S., Han, B., 2015. Learning deconvolution network for semantic segmentation, in: *Proceedings of the IEEE International Conference on Computer Vision*. pp. 1520–1528.
- Patenaude, B., Smith, S.M., Kennedy, D.N., Jenkinson, M., 2011. A Bayesian model of shape and appearance for subcortical brain segmentation. *Neuroimage* 56, 907–922.
- Raznahan, A., Greenstein, D., Lee, N.R., Clasen, L.S., Giedd, J.N., 2012. Prenatal growth in humans and postnatal brain maturation into late adolescence. *Proc. Natl. Acad. Sci.* 109, 11366–11371.
- Rohlfing, T., Brandt, R., Menzel, R., Russakoff, D., Maurer, C., 2005. Quo vadis, atlas-based segmentation? *Handb. Biomed. Image Anal.* 435–486.
- Ronneberger, O., Fischer, P., Brox, T., 2015. U-Net: Convolutional Networks for Biomedical Image Segmentation, in: *Medical Image Computing and Computer-Assisted Intervention (MICCAI)*.
- Shaw, P., Greenstein, D., Lerch, J., Clasen, L., Lenroot, R., Gogtay, N., Evans, A., Rapoport, J., Giedd, J., 2006. Intellectual ability and cortical development in children and adolescents. *Nature* 440, 676.
- Svarer, C., Madsen, K., Hasselbalch, S.G., Pinborg, L.H., Haugbøl, S., Frøkjær, V.G., Holm, S., Paulson, O.B., Knudsen, G.M., 2005. MR-based automatic delineation of volumes of interest in human brain PET images using probability maps. *Neuroimage* 24, 969–979.

- Vedaldi, A., Lenc, K., 2015. Matconvnet: Convolutional neural networks for matlab, in: Proceedings of the 23rd ACM International Conference on Multimedia. ACM, pp. 689–692.
- Wachinger, C., Reuter, M., Klein, T., 2017. DeepNAT: Deep convolutional neural network for segmenting neuroanatomy. *NeuroImage*.
- Wachinger, C., Salat, D.H., Weiner, M., Reuter, M., Initiative, A.D.N., 2016. Whole-brain analysis reveals increased neuroanatomical asymmetries in dementia for hippocampus and amygdala. *Brain* 139, 3253–3266.
- Wang, H., Yushkevich, P.A., 2013. Multi-atlas segmentation with joint label fusion and corrective learning—an open source implementation. *Front. Neuroinformatics* 7.

Table 1: Summary of the experiments for evaluating segmentation accuracy (1-5) and reliability (6-8). For each experiment, the table indicates the datasets used for pre-training, fine-tuning and testing together with the number of scans in parentheses. We also list the purpose for each experiment.

Evaluation	Experiment Number	Pre-Training	Fine-Tuning	Testing	Purpose of Experiment	
Segmentation Accuracy	Experiment 1	IXI (581)	MALC (15)	MALC (15)	Benchmark Challenge Data	
	Experiment 2		MALC (28)	ADNI (29)	Robustness to pathology, scanner field strength, group analysis by effect sizes.	
	Experiment 3			IBSR (18)	Robustness to low resolution data with wide age range.	
	Experiment 4			CANDI (13)	Robustness to children with psychological disorders.	
	Experiment 5			HarP (131)	Robustness of hippocampus segmentation in presence of dementia.	
Experiment 6	ALVIN (16)			Reliable volume estimation of lateral ventricles for young and aged subjects (dementia).		
Segmentation Reliability	Experiment 7		IXI (581)	MALC (28)	TRT (120)	Inter- and intra-session reliability.
	Experiment 8				HTP (67)	Reliability across 8 centers with different scanners.

Table 2: Effect sizes (Hedge's  $g$  and Glass  $\Delta$ ) with confidence intervals from manual segmentation, QuickNAT and FreeSurfer for the ADNI-29 dataset between controls and AD. The groups consist of 15 control and 14 AD subjects.

	Hedge's $g$		
	Manual	QuickNAT	FreeSurfer
Hippocampus left	1.22 (0.37 - 1.99)	1.18 (0.34 - 1.95)	1.00 (0.18 - 1.76)
Amygdala left	1.11 (0.28 - 1.88)	1.16 (0.32 - 1.94)	0.92 (0.12 - 1.68)
Hippocampus right	1.26 (0.41 - 2.04)	1.25 (0.40 - 2.03)	1.06 (0.24 - 1.18)
Amygdala right	1.26 (0.41 - 2.04)	1.40 (0.53 - 2.20)	0.96 (0.15 - 1.72)
	Glass $\Delta$		
	Manual	QuickNAT	FreeSurfer
Hippocampus left	0.96 (0.11 - 1.81)	0.88 (0.05 - 1.72)	0.75 (0.05 - 1.57)
Amygdala left	0.94 (0.09 - 1.79)	0.93 (0.09 - 1.77)	0.83 (0.00 - 1.65)
Hippocampus right	1.00 (0.14 - 1.85)	0.97 (0.12 - 1.82)	0.83 (0.00 - 1.66)
Amygdala right	1.03 (0.17 - 1.89)	1.09 (0.22 - 1.95)	0.79 (0.03 - 1.61)

Table 3: Results of reliability evaluation in experiments 7 and 8 for QuickNAT and FreeSurfer. (A) Inter-session coefficient of variation on Test-Retest (TRT) dataset (experiment 7). (B) RMS CV coefficient of variation for Human Traveling Phantom (HTP) dataset across 8 sites for 5 subjects. Lower values indicate higher reliability and are marked in bold face.

A) TRT Dataset

Structures	Inter-session CVt (%)	
	FreeSurfer	QuickNAT
Hippocampus	2.92	<b>0.80</b>
Lateral Ventricles	3.40	<b>3.04</b>
Amygdala	5.21	<b>2.39</b>
Putamen	3.92	<b>0.85</b>
Pallidum	5.42	<b>1.42</b>
Caudate	1.58	<b>1.14</b>
Thalamus	6.06	<b>0.93</b>
Cerebral WM	<b>0.87</b>	1.91

B) HTP Dataset

Structures	RMS CV (%)	
	FreeSurfer	QuickNAT
Hippocampus	4.47	<b>3.02</b>
Lateral Ventricles	<b>7.45</b>	10.9
Amygdala	<b>4.15</b>	6.29
Putamen	6.31	<b>3.63</b>
Pallidum	7.98	<b>3.12</b>
Caudate	<b>3.44</b>	8.18
Thalamus	3.65	<b>2.35</b>
Cerebral WM	<b>2.86</b>	3.99

Figure 1: Illustration of the two-step training strategy for QuickNAT. First, we use an existing segmentation software (e.g., FreeSurfer) to automatically segment a large unlabeled corpus (IXI Dataset with 581 scans). These labels are referred to as auxiliary labels and used to pre-train QuickNAT. Second, we fine-tune the network on 28 scans from the multi-atlas label challenge, which were manually annotated by an expert. Fine-tuning does not start from scratch, but continues optimizing the pre-trained model from step 1, to maximally benefit from the scarce data with manual annotations.

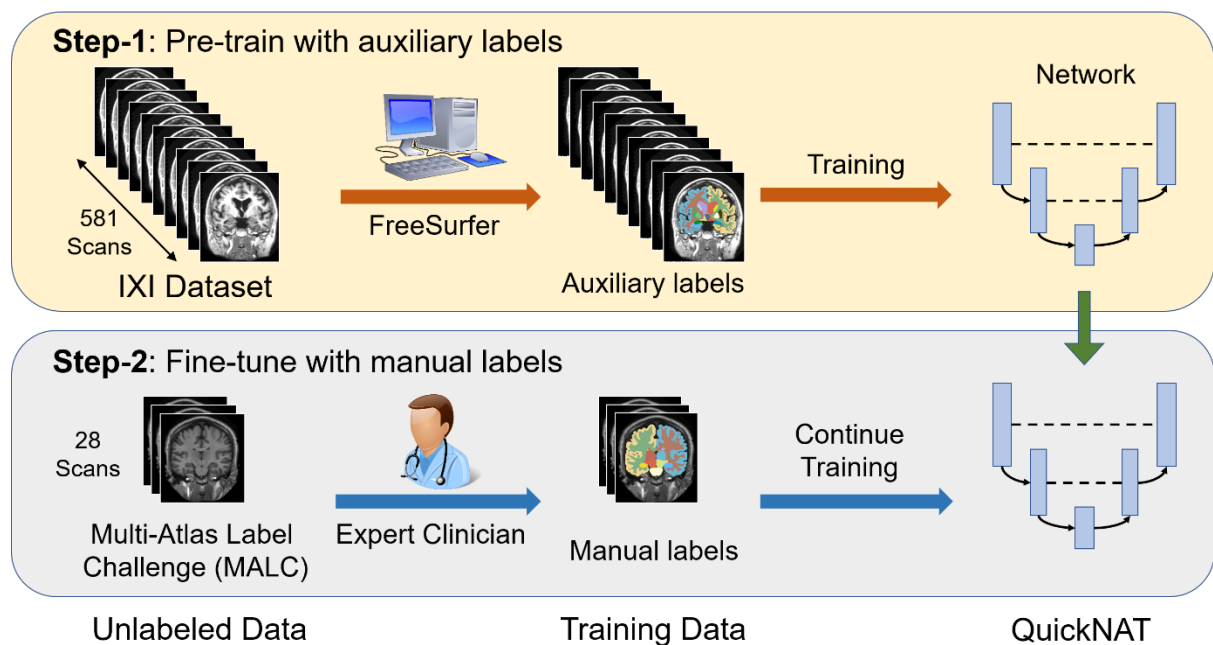


Figure 2: Fig. 2(a) illustrates QuickNAT's encoder-decoder based fully convolutional architecture consisting of dense blocks, shown in the zoomed view. The symbols corresponding to different network layers are also explained here. Fig. 2(b) shows the multi-view aggregation step that combines segmentations from models trained on 2D slices along three principle axes: coronal, sagittal and axial. The final segmentation is obtained by combining the probability maps from all the three networks.

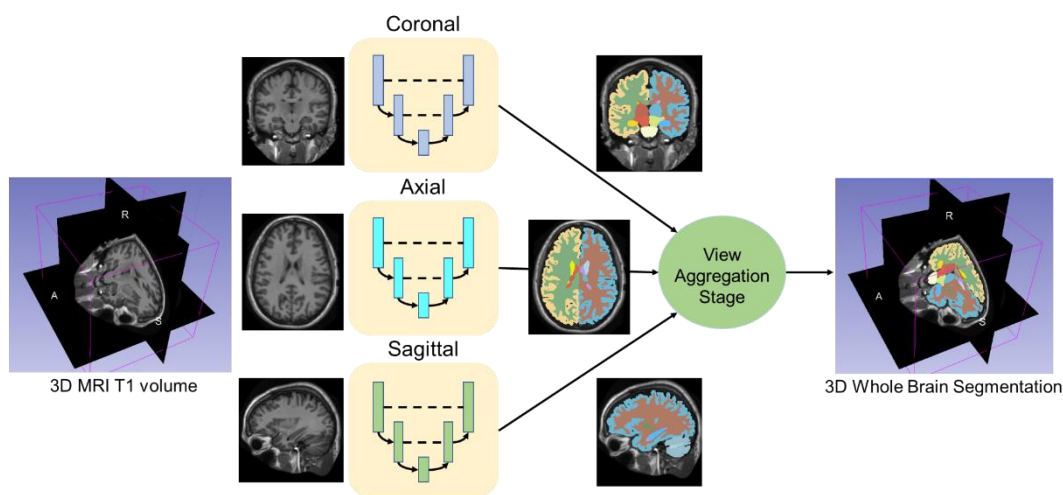
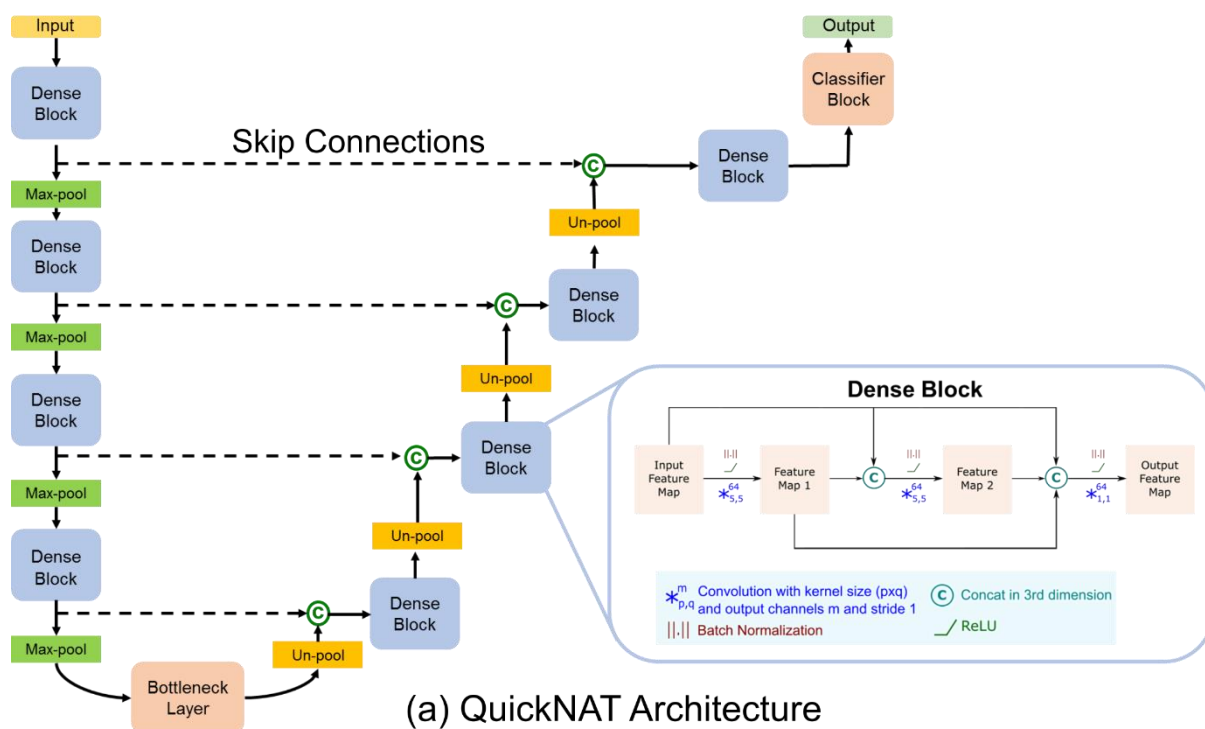


Figure 3: Segmentation results on the MALC dataset for whole brain segmentation. (a) presents a box-plot with structure-wise Dice scores of the left hemisphere for QuickNAT, PICSL, Spatial STAPLE and U-Net for 15 Testing subjects. The structures where QuickNAT outperforms any of the other methods by a statistically significant margin is indicated by a star (\*) of their respective colors estimated using two-sided Wilcoxon rank-sum test. (b) compares qualitative results of QuickNAT trained with and without pre-training along with PICSL. A zoomed view shows left Putamen (dark brown) and left Pallidum (white) with a white arrow for all the cases indicating the superior segmentation performance of fine-tuned QuickNAT over others. (c) presents the illustration of segmentation speed for QuickNAT, DeepNAT, FreeSurfer and PICSL in log scale, demonstrating its superior speed.

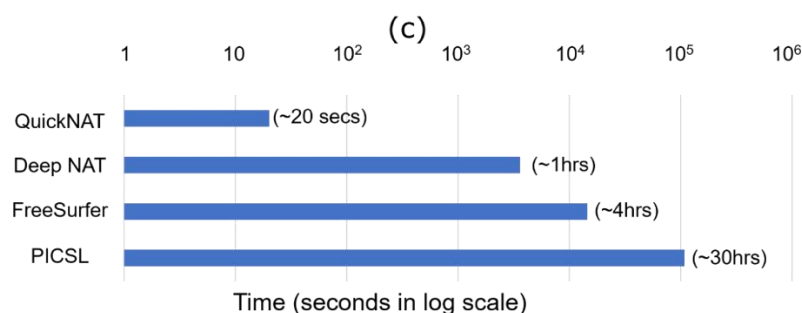
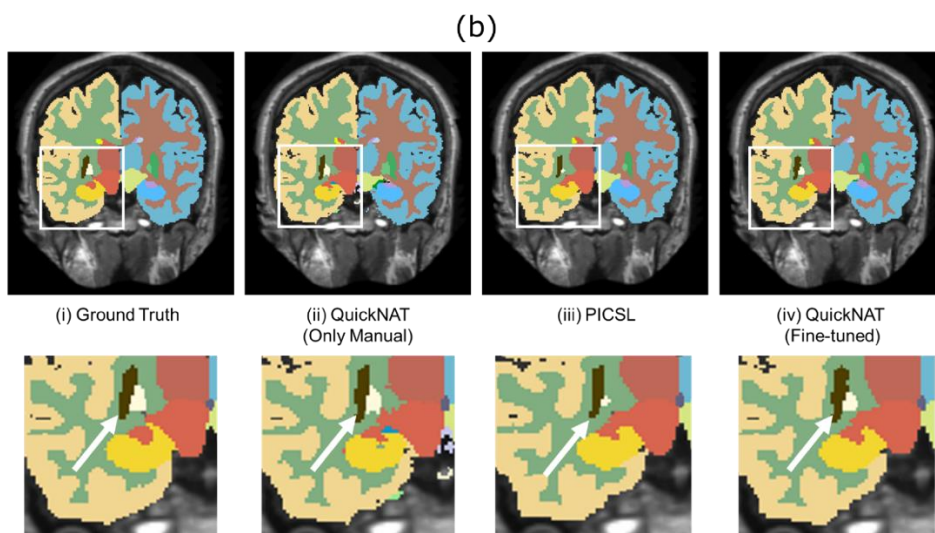
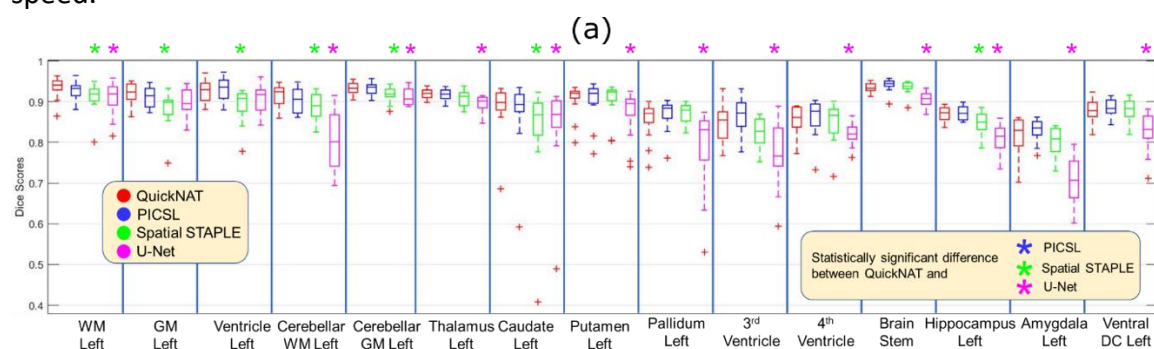




Figure 4: Structure-wise Dice scores of the left hemisphere for ADNI-29 dataset for whole brain segmentation, where QuickNAT is compared against FreeSurfer. All the 29 subject scans were used for testing. Statistically significant differences ( $p < 0.05$ ) are indicated by star (\*). The p-values were estimated using two-sided Wilcoxon rank-sum test.

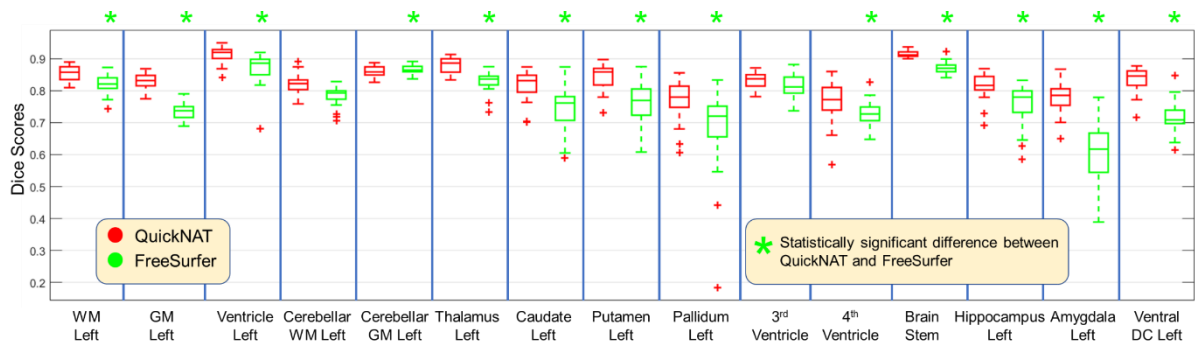


Figure 5: Boxplot of Dice scores. (a) Comparison of Dice scores for 1.5 Tesla and 3.0 Tesla field strengths for QuickNAT and FreeSurfer on ADNI-29. 15 scans were acquired at 1.5T and 14 scans at 3T. (b) Comparison of Dice scores for AD and controls for QuickNAT and FreeSurfer on ADNI-29. 15 scans were acquired from controls and 14 from AD. The p-values were estimated using two-sided Wilcoxon rank-sum test.

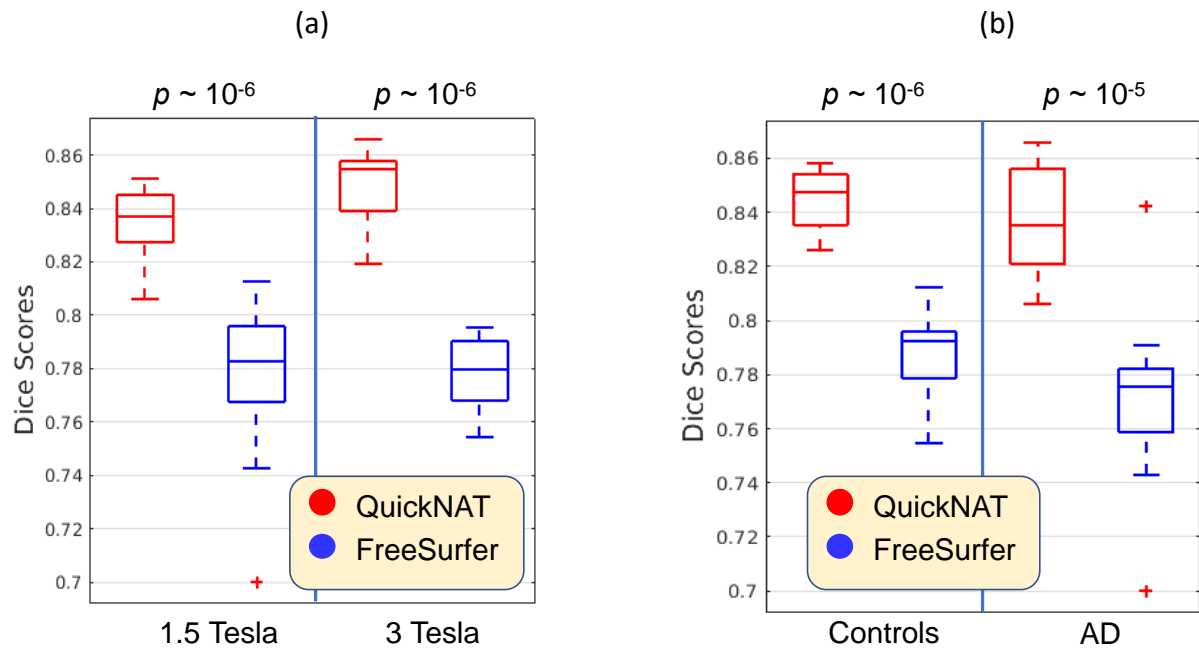


Figure 6: Structure-wise Dice scores of the left hemisphere for IBSR dataset for whole brain segmentation, where QuickNAT is compared against FreeSurfer. All the 18 scans from the dataset are exclusively used for testing. Statistically significant differences ( $p < 0.05$ ) are indicated by star (\*). The p-values were estimated using two-sided Wilcoxon rank-sum test.

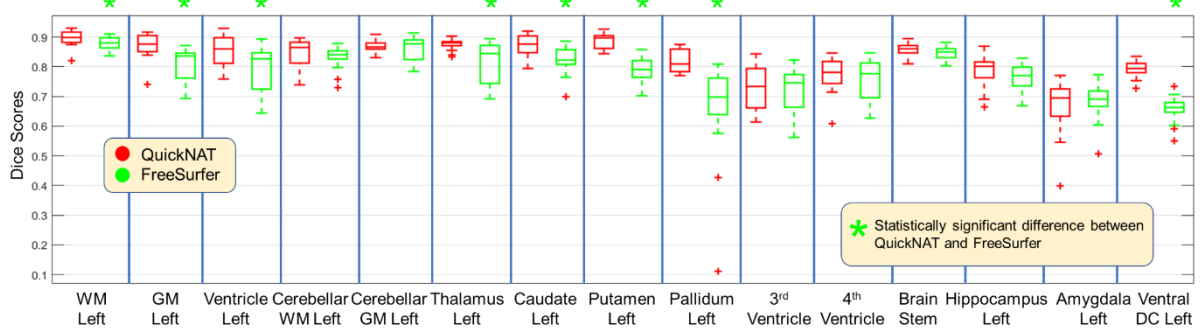


Figure 7: Structure-wise Dice scores of the left hemisphere for CANDI dataset for whole brain segmentation, where QuickNAT is compared against FreeSurfer. All the 13 scans from the dataset are exclusively used for testing. Statistically significant differences ( $p < 0.05$ ) are indicated by star (\*). The p-values were estimated using two-sided Wilcoxon rank-sum test.

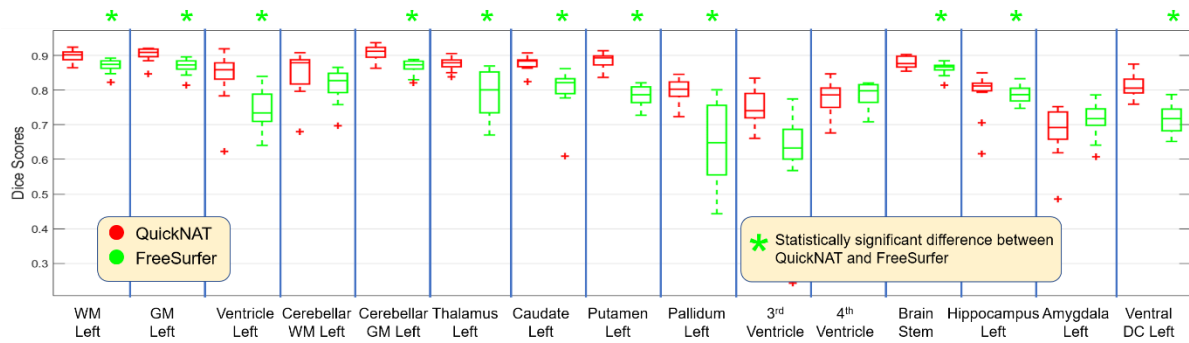
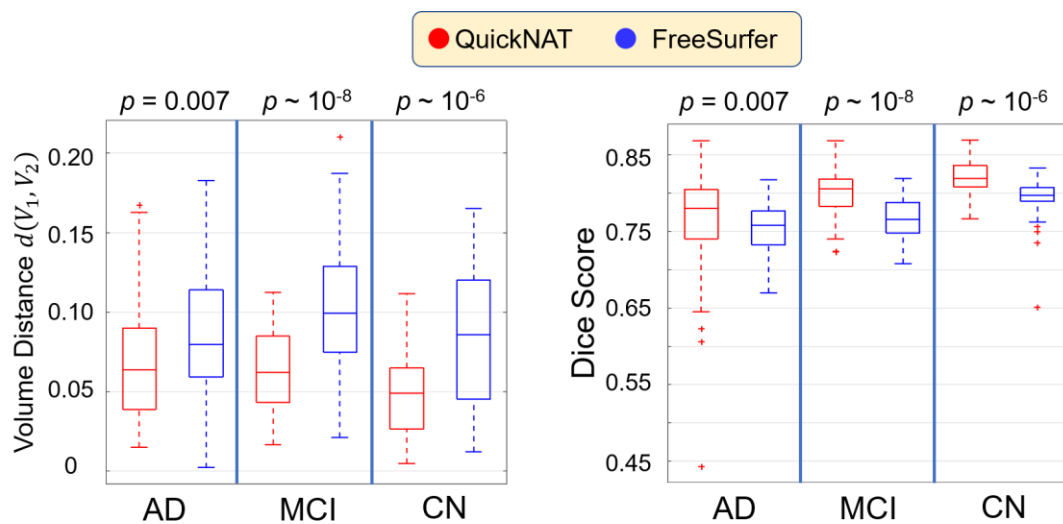
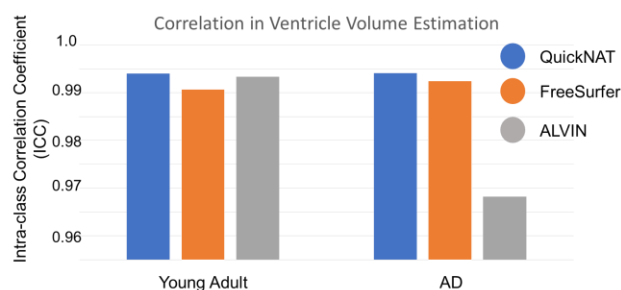


Figure 8: Results on HarP and ALVIN datasets. Fig. 8 (a) shows hippocampus segmentation performance on the HarP dataset, in terms of Dice score and volume distance for different diagnoses (42 Controls, 44 MCI, and 45 AD). Higher Dice score and correlation indicates better performance, while lower volume distance indicates better performance. The p-values were computed using two-sided Wilcoxon rank-sum test. Fig. 8 (b) illustrates the performance of QuickNAT for ventricle volume estimation after segmentation and compares to FreeSurfer and ALVIN, on the dataset introduced by ALVIN. The performance is evaluated by estimating intra-class correlation (metric used in (Kempton et al., 2011)) for both young adults (7 scans) and AD subjects (9 scans).



(a) Hippocampus Segmentation (HarP)



(b) Lateral Ventricle Segmentation (ALVIN)

## Supplementary Material

QuickNAT: Segmenting MRI Neuroanatomy in 20 seconds  
A. Guha Roy, S. Conjeti, N. Navab, C. Wachinger

### Supplementary Datasets

We use **nine brain MRI datasets** in our experiments. Five of them contain manual annotations, were used to evaluate segmentation accuracy. Three datasets were used for testing reliability of the segmentation framework. Supplementary Table 1 summarizes the number of subjects per dataset, the age range, the diagnosis, and the annotated structures. Present diagnoses are Alzheimer's disease (AD) and mild cognitive impairment (MCI). Details about acquisition protocol used in each of the datasets can be found in their respective references. All MRI datasets used are publicly available.

**IXI dataset:** The dataset is collected from 3 different hospitals from London (Hammersmith hospital, Guy's hospital, institute of psychiatry) and consists of both 1.5T and 3.0T MRI T1 scans for 581 healthy subjects. The data was collected by Imperial College London and is available for download at <http://brain-development.org/ixi-dataset/>.

**Multi-Atlas Labelling Challenge (MALC):** The dataset is part of the OASIS dataset (Marcus et al., 2007) and contains MRI T1 scans from 30 subjects with manual annotations for the whole brain (Landman and Warfield, 2012). In the challenge, 15 volumes were defined for training and 15 for testing. We follow the same setup in our experiments. The dataset also includes follow-up scans from 5 subjects to evaluate inter-run consistency. The manual segmentations were provided by Neuromorphometrics, Inc. under academic subscription.

**ADNI-29:** The dataset is a subset of 29 subjects from the Alzheimer's Disease Neuroimaging Initiative (ADNI, [adni.loni.usc.edu](http://adni.loni.usc.edu)). The primary goal of ADNI has been to test whether serial MRI, PET, other biological markers, and clinical and neuropsychological assessment can be combined to measure the progression of MCI and AD. Manual whole-brain segmentations were provided by Neuromorphometrics, Inc. under academic subscription. The dataset includes 15 controls and 14 Alzheimer's patients. Further, 15 scans were acquired with 1.5T field strength and 14 scans with 3.0T, with balanced distribution of AD and controls.

**Internet Brain Segmentation Repository (IBSR):** The dataset consists of 18 T1 MRI scans with manual segmentations of the whole brain. The MR scans and their manual segmentations were provided by the Center for Morphometric Analysis at Massachusetts General Hospital and are available at <http://www.cma.mgh.harvard.edu/ibsr/>.

**Child and Adolescent NeuroDevelopment Initiative (CANDI):** The dataset consists of 13 T1 MRI scans (8 male, 5 female) of children with psychiatric disorders, having minimum age of 5, maximum age of 15 and mean age of 10 years. Manual whole-brain segmentations were provided by Neuromorphometrics, Inc. under academic subscription. The dataset is publicly available at (Kennedy et al., 2012).

**Harmonized Protocol (HarP):** The European Alzheimer's Disease Consortium and ADNI together provided a Harmonized Protocol (HarP) for manual hippocampal segmentation from MRI (Boccardi et al., 2015). It was defined through an evidence-based Delphi panel that converged on a consensus definition. After standardization, a dataset with 131 volumes was released with manually annotated right/left hippocampus for development and evaluation of standard automated hippocampus segmentation algorithms. Special attention was paid for ensuring that the dataset is representative of physiological and pathological variability (age, dementia severity), field strength (1.5T and 3T) and scanner manufacturer (GE, Philips and Siemens). 45 scans were from AD subjects, 42 scans from Controls and 44 scans from MCI.

**ALVIN:** (Kempton et al., 2011) released the ALVIN dataset in an attempt to standardize the evaluation of segmentation algorithms. The dataset consists of 7 young adult subjects and 9 subjects with Alzheimer's disease. The dataset does not provide manual segmentations but volume measurements of the ventricles. These volume measurements are available from a manual rater at two points of time to observe intra-observer variability.

**Test-Retest (TRT) dataset:** This dataset was released to analyze reliability of segmentation frameworks for estimating volumes of brain structures (Maclaren et al., 2014). The dataset consists of 120 MRI T1 scans from 3 subjects (40 scans per subject) in 20 sessions (2 scans per session) over the duration of 31 days. All the subjects were healthy with ages within 26-31 years.

**Travelling Human Phantom (THP) dataset:** This dataset was released to check the reliability of automated segmentation frameworks in estimating volumes from scans acquired from different sites (Magnotta et al., 2012). In the study, 3 healthy subjects were scanned at 8 different centers in the USA using scanners from different vendors. All scans were acquired within a period of 30 days. The sites are:

1. Cleveland Clinic
2. Dartmouth
3. University of Iowa
4. Johns Hopkins
5. Massachusetts General Hospital
6. University of California Irvine
7. University of Minnesota
8. University of Washington.

Supplementary Table 1: Summary of the datasets used for training and testing. Dataset characteristics are shown together with available manually annotated structures.

Dataset	No. of Subjects	Age range of Subjects (mean $\pm$ std)	Diagnosis	Annotated Structures
IXI	581	49.09 $\pm$ 16.43	Normal	None
MALC	30	34.16 $\pm$ 20.40	CN/AD/MCI	Whole Brain
ADNI-29	29	75.87 $\pm$ 5.86	CN/AD	Whole Brain
IBSR	18	29.05 $\pm$ 4.80	-	Whole Brain
CANDI	13	10.00 $\pm$ 3.13	Psychiatric Disorders	Whole Brain
ALVIN	16	AD: 77.4 $\pm$ 2.4 Young adults: 23.8 $\pm$ 4.1	CN/AD	Lateral Ventricle
HarP	131	AD: 74.2 $\pm$ 7.8 CN: 76.2 $\pm$ 7.4 MCI: 74.7 $\pm$ 8.1	CN/MCI/AD	Hippocampus
TRT	3 (40 scans/subject)	26-31	Normal	None
THP	5 (Scans from 8 sites in USA)	-	Normal	None

It must be noted that

- The sample size for the experiments were based on the number of scans available on the publicly available benchmark neuroimaging (MRI T1) dataset.
- No extra exclusion criteria were imposed for this study. Any exclusion criteria from the respective imaging benchmark holds.
- The reproducibility of the proposed tool was investigated on various platforms (Windows 10, Ubuntu 14.04/16.04) with variants of NVIDIA GPU with CUDA compatibility (Titan X Pascal, Titan Xp, Tesla K40, GTX 960M). Identical results were obtained.
- No additional stratification was performed for the experiments. Prior grouping strategies from the respective benchmark datasets holds.
- The Investigators of this study were not involved in any capacity for the data acquisition and annotation, so were blinded to group allocation.
- No prior pre-processing was performed on the data for all the experiments.
- Each experiment was performed 10 times for checking consistency of the results. Identical results were observed. Any variation in results can only arise from numerical approximation which was observed to be negligible for our case.



## Supplementary Experiments

In the following, we describe the experiments in details. **In experiments 2-8, we do not re-train QuickNAT but only deploy the model to get realistic robustness measures on unseen datasets (Table 1).** The datasets contain scans from different scanner manufacturers and field strengths (1.5T and 3.0T), together with subjects from a wide age range and pathologies (AD/MCI/CN), to provide a diverse testing scenario. Performance measures are Dice score, volume distance, intra-class correlation and coefficient of variation. The non-parametric two-sided Wilcoxon rank-sum test is used to evaluate significance. We evaluate segmentation accuracy in experiments 1-5, and reliability in experiments 6-8 (Table 1).

### Experiments for segmentation accuracy

#### Experiment 1: Multi-Atlas Labelling Challenge (MALC)

In the first experiment, we use the MALC data and replicate the setup of the original challenge (Landman and Warfield, 2012). A problem associated with segmenting this dataset is that all the training volumes are from young adults while testing volumes include subjects with 70 years and older, maximum 90 years. To achieve good performance, the network therefore has to be robust across differently aged subjects.

In this experiment, we compare the performance of QuickNAT with state-of-the-art methods and we also evaluate the impact of pre-training. Supplementary Table 2 reports the results measured in Dice overlap (Online Methods). First, we compare with the F-CNN models (FCN, U-Net). Along each row, we observe that for all the F-CNN models, pre-training with auxiliary labels followed by fine-tuning (termed as ‘Fine-tuned’ in Supplementary Table 2) yields significantly ( $p < 0.001$ ) better performance than training only with limited manually annotated data (termed as ‘Only Manual’ in Supplementary Table 2). Second, when comparing across columns, we observe that QuickNAT performs better than U-Net and FCN, not only for imitating the FreeSurfer labels in the pre-trained model, but also when trained with limited manually annotated data exclusively and the final fine-tuned model. Finally, QuickNAT significantly ( $p < 0.001$ ) outperforms U-Net and FCN by a margin of 5% and 12% mean dice score.

Supplementary Table 2: Comparison of Dice scores of QuickNAT with state-of-the-art methods on 15 testing scans from MALC.

	<b>Pre-Trained *</b>	<b>Only Manual *</b>	<b>Fine-tuned *</b>
<b>QuickNAT</b>	0.798 ± 0.097	0.874 ± 0.067	<b>0.901 ± 0.045</b>
<b>U-Net</b>	0.681 ± 0.193	0.762 ± 0.124	0.857 ± 0.079
<b>FCN</b>	0.579 ± 0.245	0.534 ± 0.311	0.778 ± 0.121
<b>DeepNAT</b>	0.891 for 25 structures		
<b>Spatial STAPLE</b>	0.879 ± 0.063		
<b>PICSL</b>	0.898 ± 0.050		

\* Results of only using the pre-trained model on test data is referred as ‘**Pre-Trained**’. Results for training only with 15 manual data from scratch is referred as ‘**Only Manual**’. Results of using the pre-trained model and fine-tune it with 15 manual data is referred as ‘**Fine-tuned**’.

Next, we compare the final QuickNAT model with state-of-the-art atlas-based methods PICS (Wang and Yushkevich, 2013) and Spatial STAPLE (Asman and Landman, 2012), and state-of-the-art 3D CNN based deep learning method DeepNAT (Wachinger et al., 2017). Our model outperforms Spatial STAPLE by a statistically significant margin ( $p < 0.05$ ). It outperforms PICS by a small margin which is not statistically significant. It also outperforms DeepNAT when compared for segmentation for only 25 structures. DeepNAT operates in 3D, however, on patches extracted from the image, which limits the context for the prediction. A direct extension to a 3D full volume prediction, instead of patches, is restricted by the current GPU memory.

Next to the comparison of brain-wide Dice scores, we show a structure-wise comparison in Supplementary Figure 1. Significant differences are highlighted with a star symbol (\*). No significant differences exist across any of the 27 structures to the challenge winner PICS. QuickNAT has significantly higher Dice for many structures compared to Spatial STAPLE (14 of 27) and U-Net (23 of 27). Notable is the good performance of QuickNAT for gray and white matter, which is a likely consequence that the learning-based approaches do not rely on a homology to exist between test and training volumes.

### **Qualitative Analysis**

Sample segmentations are visualized in Fig. 3 (b) for QuickNAT (trained on limited data), PICS and QuickNAT (fine-tuned) along with the manual segmentation. A zoomed region of the segmentations is also presented. We indicate two important sub-cortical structures left putamen (brown) and left pallidum (white) with a white arrow. We can observe that left putamen is under segmented for PICS. We also observe many spurious misclassified regions in the background in QuickNAT (trained with limited data), which is not present for QuickNAT (fine-tuned).

### **Speed**

Existing state-of-the-art atlas-based brain segmentation frameworks build upon 3D deformable volume registration, e.g., ANTs (Avants et al., 2011). In pair-wise registrations, each image in the atlas is transformed to the test image. This results in long runtimes, since a single pair-wise registration takes about 2 hours on a 2GHz CPU machine (Landman and Warfield, 2012). On MALC with 15 training images, the approximate segmentation time for both PICS and Spatial STAPLE is 30h/vol. FreeSurfer has its own atlas and takes around 4h/vol. DeepNAT uses a 3D patch based approach for segmentation taking around 1h/vol. In comparison to these models, QuickNAT segments a volume in 20s, which is orders of magnitude faster. We illustrate the segmentation time in Fig. 3c in logarithmic scale. The speed of QuickNAT can be further reduced to about 6s, if only one anatomical view instead of all three are used for segmentation. The best segmentation performance on a single view is observed for coronal view, which results in an overall Dice of  $0.895 \pm 0.055$  compared to  $0.901 \pm 0.045$  with view aggregation.

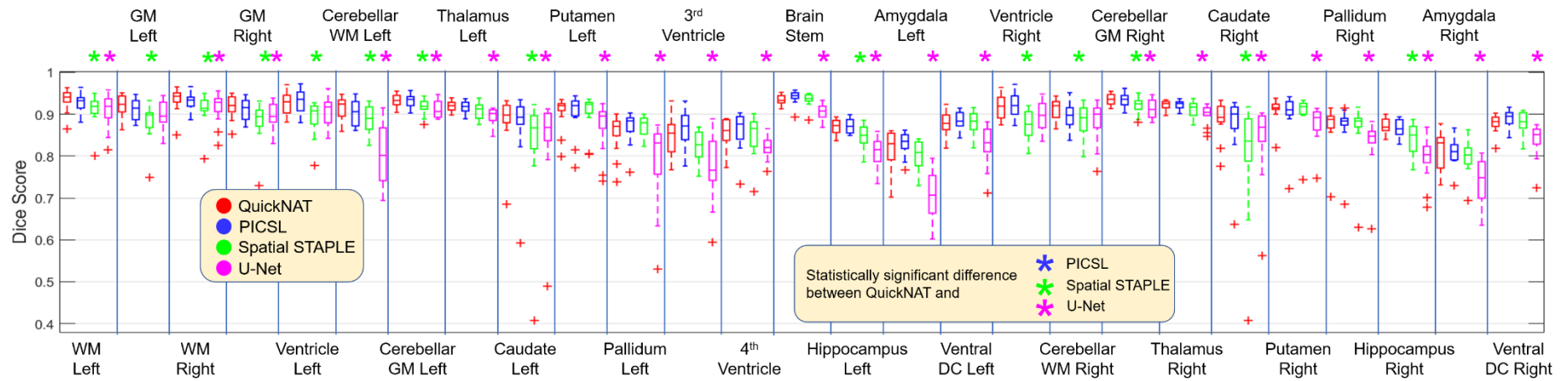
### **Inter-Run Consistency (Supplementary Table 3)**

MALC includes a second MRI T1 scan for 5 patients to evaluate the consistency of the segmentation algorithm across acquisitions (test/retest). For quantification, we estimate the volumes of different structures for both runs and compute the volume distance between them (Online Methods). Supplementary Table 3 reports mean volume distance for

whole brain, hippocampus, amygdala, lateral ventricles, white matter and grey matter; comparing QuickNAT with PICSL and Spatial STAPLE. In case of whole brain, all values are very low with low standard deviation, indicating that each the methods produces highly consistent results. For structures hippocampus, white matter, grey matter QuickNAT has a lower volume distance indicating its superiority over PICSL and Spatial STAPLE. For structures Lateral ventricle and amygdala, QuickNAT has poorer performance than PICSL and Spatial STAPLE, but within an acceptable range of 2-3%.

Supplementary Table 3: Inter-Run Consistency reported by volume distance over 5 subjects from MALC Dataset chosen by the Challenge organizers.

<b>Method</b>	<b>Whole Brain</b>	<b>Hippocampus</b>	<b>Amygdala</b>	<b>Lateral Ventricles</b>	<b>White Matter</b>	<b>Grey Matter</b>
<b>QuickNAT</b>	0.017 ± 0.016	0.020 ± 0.012	0.025 ± 0.012	0.032 ± 0.025	0.005 ± 0.004	0.009 ± 0.006
<b>PICSL</b>	0.018 ± 0.018	0.041 ± 0.026	0.010 ± 0.001	0.015 ± 0.010	0.012 ± 0.005	0.019 ± 0.006
<b>Spatial STAPLE</b>	0.013 ± 0.015	0.021 ± 0.012	0.011 ± 0.009	0.012 ± 0.005	0.005 ± 0.004	0.011 ± 0.011



Supplementary Figure 1: Box-plot of Dice scores comparing QuickNAT with PICSL, Spatial STAPLE and U-Net on 15 test volumes of MALC dataset for all the 27 structures. Statistical significance ( $p < 0.05$ ) in comparison to QuickNAT is indicated by a star symbol (\*). The p-values were estimates using two-sided Wilcoxon rank-sum test. WM indicates White Matter and GM indicates Grey Matter.

We fine-tuned the pre-trained QuickNAT model with 28 manually annotated MALC scans to get our final model. This trained model is deployed on other unseen datasets in experiment 2-8 to evaluate its robustness (Table 1).

### Experiment 2: ADNI-29

ADNI-29 contains whole brain segmentations for 14 AD patients and 15 controls from the ADNI dataset (Jack et al., 2008). The dataset contains 15 1.5T scans and 14 3.0T scans. Next, to measuring segmentation accuracy, we also use this dataset to evaluate the performance of QuickNAT in group analysis by computing effect sizes and  $p$ -values. ADNI is one of the largest longitudinal MRI studies and the segmentation of the scans is of high medical relevance. We segmented all the 29 scans by deploying the already trained QuickNAT model.

We present the mean Dice Score on the dataset, comparing QuickNAT and FreeSurfer in Supplementary Table 4. QuickNAT outperforms FreeSurfer by 6% in Dice Score with  $p < 10^{-7}$ . Also, a structure-wise comparison is provided in Supplementary Fig. 2, where QuickNAT has significantly higher dice score than FreeSurfer for 24 out of 27 structures.

Supplementary Table 4: Dice score on the ADNI-29 dataset with 29 scans shows significance difference ( $p < 10^{-7}$ ) between QuickNAT and FreeSurfer.

Method	Mean Dice Score (SD)
<b>QuickNAT</b>	0.841 ± 0.064
<b>FreeSurfer</b>	0.778 ± 0.097

Supplementary Tables 5 and 6 reports the effect sizes and  $p$ -values, respectively, for the group analysis of comparing AD with controls. We only report the values for the hippocampus and amygdala due to their important role in AD pathology. The analyses are performed on volume estimates, where we normalize volume estimates by the intracranial volume. For computing effect sizes, we use Hedge's  $g$  and Glass  $\Delta$ . Since we have less than 50 subjects for each of the groups, we use variants of these metrics, customized for small samples. We report effect sizes and corresponding confidence intervals, computed on the manual segmentations together with those from QuickNAT and FreeSurfer. We observe that for both metrics, QuickNAT is closer to the actual estimate than FreeSurfer.

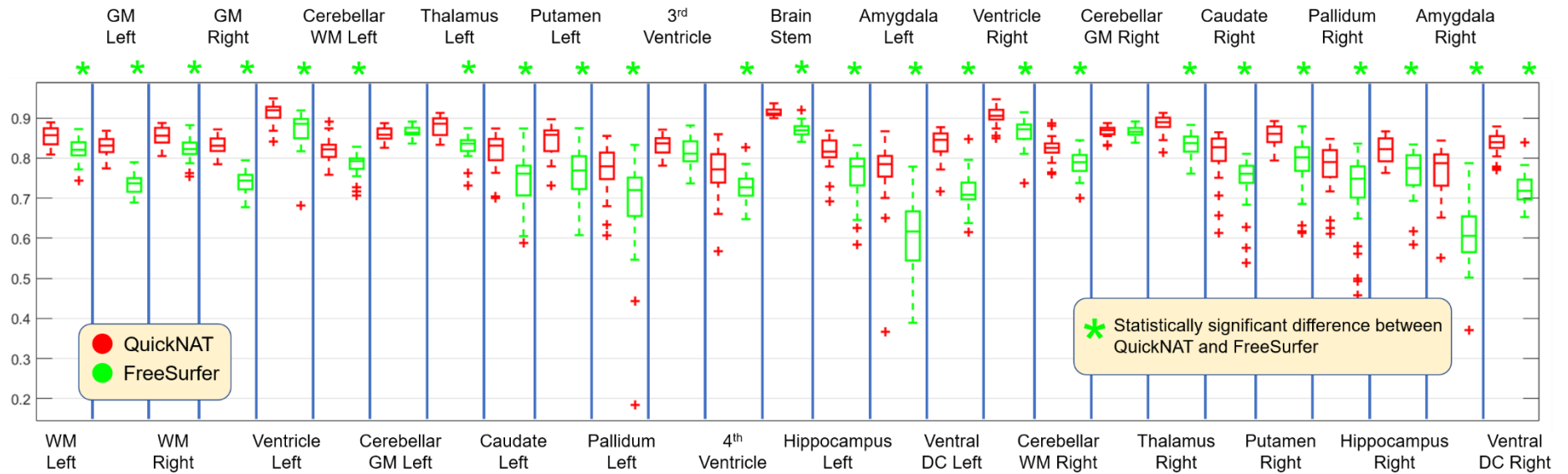
We also compare the performance of QuickNAT in finding significant associations between diagnostic groups and brain morphology. Towards this, we use a standard linear regression model:  $\text{Volume} \sim \text{Age} + \text{Sex} + \text{Diagnosis}$ , and compare the  $p$ -values of the variable diagnosis, in Supplementary Table 6. The  $p$ -values of QuickNAT are closer to the ones from the manual segmentation.

Supplementary Table 5: Effect sizes and confidence intervals from manual segmentation, QuickNAT and FreeSurfer in terms of Hedge's  $g$  and Glass  $\Delta$  for ADNI-29 dataset between controls and AD.

	Hedge's $g$		
	Manual	QuickNAT	FreeSurfer
Hippocampus left	1.22 (0.37 - 1.99)	1.18 (0.34 - 1.95)	1.00 (0.18 - 1.76)
Amygdala left	1.11 (0.28 - 1.88)	1.16 (0.32 - 1.94)	0.92 (0.12 - 1.68)
Hippocampus right	1.26 (0.41 - 2.04)	1.25 (0.40 - 2.03)	1.06 (0.24 - 1.18)
Amygdala right	1.26 (0.41 - 2.04)	1.40 (0.53 - 2.20)	0.96 (0.15 - 1.72)
	Glass $\Delta$		
	Manual	QuickNAT	FreeSurfer
Hippocampus left	0.96 (0.11 - 1.81)	0.88 (0.05 - 1.72)	0.75 (0.05 - 1.57)
Amygdala left	0.94 (0.09 - 1.79)	0.93 (0.09 - 1.77)	0.83 (0.00 - 1.65)
Hippocampus right	1.00 (0.14 - 1.85)	0.97 (0.12 - 1.82)	0.83 (0.00 - 1.66)
Amygdala right	1.03 (0.17 - 1.89)	1.09 (0.22 - 1.95)	0.79 (0.03 - 1.61)

Supplementary Table 6: Normalized volume estimates for manual, QuickNAT and FreeSurfer segmentations are used in a linear model,  $\text{Volume} \sim \text{Age} + \text{Sex} + \text{Disease}$ , for the ADNI-29 dataset. The normalized regression co-efficient and  $p$ -values corresponding to variable Disease is reported below.

	Manual	QuickNAT	FreeSurfer
Hippocampus left	1.136 (0.0012)	1.117 (0.0014)	1.015 (0.0031)
Amygdala left	1.013 (0.0058)	1.124 (0.0009)	0.954 (0.0068)
Hippocampus right	1.157 (0.0010)	1.149 (0.0011)	1.061 (0.0020)
Amygdala right	1.119 (0.0020)	1.247 (0.0002)	0.957 (0.0075)



Supplementary Figure 2: Box-plot of Dice scores comparing QuickNAT with FreeSurfer on ADNI-29 Dataset consisting of 15 Control and 14 AD subjects for all the 27 structures. Statistical significance ( $p < 0.05$ ) in comparison to QuickNAT is indicated by a star symbol (\*). The p-values were estimated using two-sided Wilcoxon rank-sum test. WM indicates White Matter and GM indicates Grey Matter.

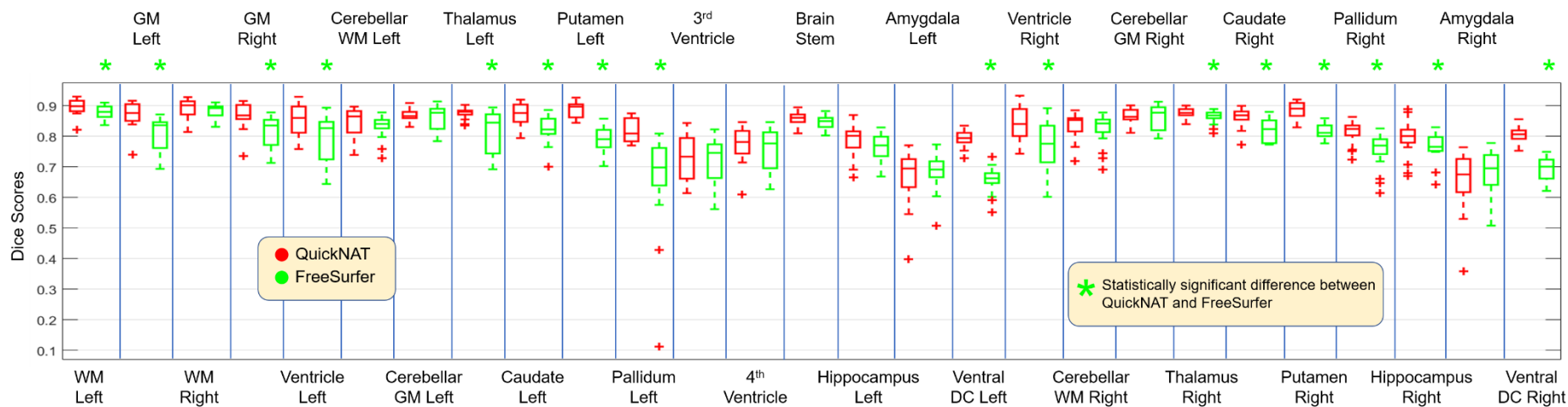
### Experiment 3: IBSR

In this experiment, we test the deployment of QuickNAT on the IBSR dataset, where the challenge is that the resolution along the anterior-superior direction is 1.5mm, which is inconsistent with isotropic 1mm resolution in the training data. Another challenge is the high variance in age of the subjects from 7 to 71 years. Supplementary Table 7 reports mean Dice scores across all structures for QuickNAT and FreeSurfer, while Supplementary Figure 3 reports structure-wise Dice scores. QuickNAT results in higher Dice scores than FreeSurfer, which is significant for the brain-wide comparison ( $p < 10^{-7}$ ) and for 16 of the 27 structures.

Supplementary Table 7: Dice score on the IBSR dataset with 18 scans shows significance difference ( $p < 10^{-7}$ ) between QuickNAT and FreeSurfer.

Method	Mean Dice Score (SD)
<b>QuickNAT</b>	0.835 ± 0.080
<b>FreeSurfer</b>	0.794 ± 0.093





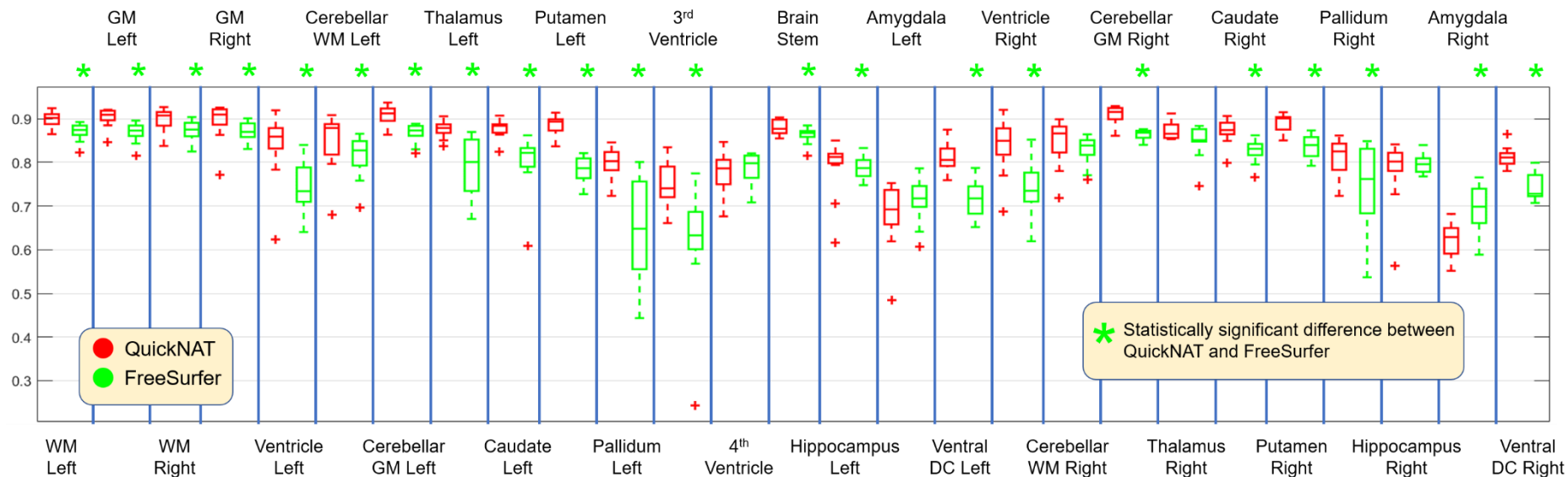
Supplementary Figure 3: Box-plot of Dice scores comparing QuickNAT with FreeSurfer on IBSR Dataset consisting of 18 MRI T1 scans for all the 27 structures. Statistical significance ( $p < 0.05$ ) in comparison to QuickNAT is indicated by a star symbol (\*). The p-values were estimated using two-sided Wilcoxon rank-sum test. WM indicates White Matter and GM indicates Grey Matter.

## Experiment 4: CANDI

A subset of 13 MRI T1 scans from the Child and Adolescent NeuroDevelopment Initiative (CANDI) dataset (Kennedy et al., 2012) with scans from children with psychiatric disorders were used as testing subjects in this experiment. The age of the subjects ranges from 5 to 15 years with a mean of 10 years. We deployed the trained QuickNAT on the dataset and compared against FreeSurfer. The challenge associated with this dataset is that the subjects of this particular age range is not used for the training set of the model (MALC). The ability of the model to generalize across unseen age ranges is investigated here. Supplementary Table 8 reports mean Dice scores across all structures for QuickNAT and FreeSurfer, while Supplementary Figure 4 reports structure-wise Dice scores. QuickNAT results in higher Dice scores than FreeSurfer, which is significant for the brain-wide comparison ( $p < 10^{-17}$ ) and for 22 of the 27 structures.

Supplementary Table 8: Dice score on the CANDI dataset with 13 scans shows significance difference ( $p < 10^{-17}$ ) between QuickNAT and FreeSurfer.

Method	Mean Dice Score (SD)
<b>QuickNAT</b>	0.842 ± 0.084
<b>FreeSurfer</b>	0.798 ± 0.092



Supplementary Figure 4: Box-plot of Dice scores comparing QuickNAT with FreeSurfer on CANDI Dataset consisting of 13 MRI T1 scans of children for all the 27 structures. Statistical significance ( $p < 0.05$ ) in comparison to QuickNAT is indicated by a star symbol (\*). The p-values were estimated using two-sided Wilcoxon rank-sum test. WM indicates White Matter and GM indicates Grey Matter.

## Comparison with FSL FIRST (for experiments 2, 3, 4)

FSL FIRST is another publicly available tool for automated segmentation of some sub-cortical structures for T1 MRI scans (Jenkinson et al., 2012; Patenaude et al., 2011). We cannot directly compare our results to FSL as it only segments 15 structures in the brain, whereas QuickNAT segments 27 structures. For a fair comparison, we selected the common 13 structures which are segmented by FSL, QuickNAT and FreeSurfer. These are **Thalamus (L+R)**, **Caudate (L+R)**, **Putamen (L+R)**, **Pallidum (L+R)**, **Hippocampus (L+R)**, **Amygdala (L+R)** and **BrainStem**. We reported the performance of QuickNAT, FreeSurfer and FSL on the 3 datasets with whole-brain ground-truth annotations (ADNI-29, CANDI, IBSR).

We observed that FSL is prone to registration errors which leads to process termination or faulty segmentations. It must be noted that the tool was deployed using its default settings for all the experiments, which was recommended in its instruction manual. FreeSurfer and QuickNAT did not produce failures. Thus, we report results once on all scans and once on those scans that FSL did not fail in Supplementary Table 9. The failure rate of FSL is higher on IBSR (44%) than on ADNI (17%) or CANDI (23%), indicating that it is susceptible to low quality scans. Considering all scans, and a sub-set of 13 structures QuickNAT outperforms both FreeSurfer and FSL by a statistically significant margin ( $p < 0.001$ ). Excluding the scans where FSL failed, QuickNAT demonstrates superior performance for ADNI-29, while FSL is best for CANDI. In IBSR, FSL outperforms QuickNAT by a small margin of 0.08% which is not statistically significant. A possible reason for the good performance of FSL on CANDI may be that FSL includes scans with age range (5-15 years) in its atlas. Scans of this age range were not included in training QuickNAT. QuickNAT can potentially show better performance on such young subjects with more training data from such age range.

Supplementary Table 9: Comparison of QuickNAT, FSL and FreeSurfer for segmentation of 13 structures common to all on ADNI-29, CANDI and IBSR Dataset. The results including and excluding scans where FSL failed are presented separately, along with the failure rate of FSL.

	Method	ADNI-29	CANDI	IBSR
All scans	QuickNAT	<b>0.825 ± 0.027</b>	<b>0.819 ± 0.028</b>	<b>0.820 ± 0.035</b>
	FreeSurfer	0.745 ± 0.042	0.780 ± 0.025	0.776 ± 0.025
	FSL	0.643 ± 0.290	0.647 ± 0.369	0.461 ± 0.419
	(Failure of FSL)	<b>5 out of 29 (17%)</b>	<b>3 out of 13 (23%)</b>	<b>8 out of 18 (44%)</b>
Scans where FSL succeeded	QuickNAT	<b>0.823 ± 0.027</b>	0.817 ± 0.032	0.817 ± 0.035
	FreeSurfer	0.745 ± 0.045	0.775 ± 0.027	0.772 ± 0.022
	FSL	0.775 ± 0.024	<b>0.841 ± 0.013</b>	<b>0.825 ± 0.013</b>

## Experiment 5: HarP Hippocampus

We evaluate the hippocampus segmentation on data released from initiatives for a harmonized protocol. Similar to ADNI-29, it is a subset of the ADNI dataset (Jack et al., 2008). The hippocampus is an important sub-cortical brain structure, whose volume and shape changes are important biomarkers for disease and aging (Bartsch and Wulff, 2015). It is also one of the most challenging structures to segment due to its small size. The HarP dataset contains 131 MRI T1 scans, which are balanced for controls, MCI and AD. The challenges associated with this dataset are: (i) subjects with neurodegenerative disease and (ii) variations in the manual annotation protocol.

Supplementary Table 10 reports results for volume distance and Dice score for controls, MCI, and AD. Figure 8 (a) presents a bar plot for the overall hippocampus segmentation scores combined for left and right. QuickNAT significantly outperforms FreeSurfer for both metrics for all diagnostic groups. QuickNAT shows the highest accuracy (highest Dice, lowest volume distance  $d$ ) on the control group. With the progression of dementia also the segmentation accuracy deteriorates. A likely reason for this behavior is that healthy subjects were used for training the network and that the brain of AD patients with severe atrophy, particularly in the hippocampus, is too different from the training set.

Supplementary Table 10: Comparison of QuickNAT with FreeSurfer for left / right hippocampus segmentation (Dice) and volume distance ( $d$ ) for 42 CN, 44 MCI and 45 AD patients on HarP dataset.

Diagnosis	Method	$d_{Left}$	$d_{Right}$	$Dice_{Left}$	$Dice_{Right}$
Controls	QuickNAT	<b>0.0536</b>	<b>0.0502</b>	<b>0.81</b>	<b>0.83</b>
	FreeSurfer	0.0943	0.0785	0.78	0.79
Mild Cognitive Impairment	QuickNAT	<b>0.0637</b>	<b>0.0616</b>	<b>0.79</b>	<b>0.81</b>
	FreeSurfer	0.1116	0.0900	0.75	0.77
Alzheimer's Disease	QuickNAT	<b>0.0727</b>	<b>0.0653</b>	<b>0.74</b>	<b>0.78</b>
	FreeSurfer	0.0933	0.0802	<b>0.74</b>	0.76

## Experiments for segmentation reliability

### Experiment 6: ALVIN Lateral Ventricle Segmentation

We follow a comprehensive testing protocol for MRI neuroanatomical segmentation techniques as proposed for lateral ventricle segmentation (Kempton et al., 2011). The dataset consists of 7 young adults and 9 patients with Alzheimer’s disease. The segmentation of lateral ventricles is important as it is an important structure for measuring the progression of neurodegenerative diseases. Lateral ventricles have been manually annotated at two time points, T1 and T2, to observe intra-observer variability and the volumes were reported. For validation, we follow the evaluation protocol by reporting intra-class correlation coefficient (ICC) (Kempton et al., 2011), in addition to volume distance  $d$ . Only volume estimates from the manual annotations are available, not the actual segmentation maps, so the Dice scores could not be computed.

Supplementary Table 11 reports the results for ALVIN (Kempton et al., 2011), FreeSurfer and QuickNAT for the young adults and the AD patients. For controls, QuickNAT shows the best performance for the first annotation and the second-best performance for the second annotation. For AD patients, QuickNAT shows the best performance for both annotations and for both ICC and volume distance. The results indicate that QuickNAT generalizes well to pathology in comparison to FreeSurfer and ALVIN for lateral ventricle segmentation.

Supplementary Table 11: Comparison of QuickNAT with FreeSurfer and ALVIN for ventricle volume estimation with manual annotations from the same rater at time points T1 and T2.

Volume distance  $d$  and intra-class correlation coefficient  $ICC$  are reported for 7 young controls and 9 Alzheimer’s disease patients.

Patient Type	Method	$d_{T1}$	$d_{T2}$	$ICC_{T1}$	$ICC_{T2}$
Young Adult (Controls)	QuickNAT	<b>0.0743</b>	0.0285	<b>0.995</b>	0.993
	FreeSurfer	0.0844	<b>0.0276</b>	0.994	0.986
	ALVIN	0.2375	0.1718	0.992	<b>0.994</b>
AD Patients	QuickNAT	<b>0.0176</b>	<b>0.0185</b>	<b>0.993</b>	<b>0.994</b>
	FreeSurfer	0.0255	0.0262	0.992	0.992
	ALVIN	0.0519	0.0558	0.968	0.968

## Experiment 7: Test-Retest (TRT) dataset

The dataset was released to test reliability of automated whole-brain segmentation algorithms in estimating volumes for some important brain structures (Maclaren et al., 2014). They acquired 120 MRI T1 scans from 3 subjects (40 scans per subject). The scans were acquired over 20 sessions (2 scans per session). All the scans were acquired within a period of 30 days. (Maclaren et al., 2014) analyzed the coefficient of variation in volume estimates within one session (intra session CVs) and the total variance over all 40 scans (CVt). Ideally as atrophy is almost negligible within the period of 30 days, the coefficient of variation in estimates should be zero. The lower the estimate, the better the estimator. We compare QuickNAT with FreeSurfer in this regard. The 8 structures considered in this experiment are consistent with the ones reported in (Maclaren et al., 2014). The results of the experiment are reported in Supplementary Table 12. Both coefficients of variation CVs and CVt are within a tolerable range of less than 2% for QuickNAT, but variations are quite high for FreeSurfer for some structures like Thalamus (~ 6%), Pallidum (~ 5%), Amygdala (~ 5%) and Putamen (~ 4%). In volume estimation of Cerebral WM, FreeSurfer exhibits a better performance than QuickNAT with (CV < 1%). A possible reason might be the sophisticated surface processing and correction stage in FreeSurfer that follows the initial segmentation.

Finally, having such low CV estimates makes QuickNAT a promising tool for group analysis studies over large datasets with reliable estimation of biomarkers. It can also be effectively used in processing longitudinal scans to model disease progression. We excluded comparison with FSL in this experiment due to FSL registration errors in some volumes.

Supplementary Table 12: Variation in volume measurement per structure. QuickNAT is compared against FreeSurfer in terms of intra-session coefficient of variation (CVs), inter-session total coefficient of variation (CVt) and the absolute difference between them. Also, the mean volume estimates per structure are reported. It must be noted that volumes of both left and right hemispheres are combined to estimate the total volume for each structure. The estimates from FreeSurfer were taken from (Maclaren et al., 2014).

Structures	Mean Volume (ml)		Intra-session CVs (%)		Inter-session CVt (%)		CVt - CVs  (%)	
	FS	Q-NAT	FS	Q-NAT	FS	Q-NAT	FS	Q-NAT
Hippocampus	8.90	7.56	2.77	<b>0.73</b>	2.92	<b>0.80</b>	0.16	<b>0.09</b>
Lateral Ventricles	10.10	14.42	<b>1.58</b>	2.33	3.40	<b>3.04</b>	1.82	<b>0.95</b>
Amygdala	3.80	2.18	4.69	<b>1.91</b>	5.21	<b>2.39</b>	0.53	<b>0.50</b>
Putamen	11.60	8.89	4.04	<b>0.71</b>	3.92	<b>0.85</b>	<b>0.13</b>	0.17
Pallidum	3.20	3.36	5.25	<b>1.32</b>	5.42	<b>1.42</b>	0.17	<b>0.12</b>
Caudate	7.40	6.82	1.54	<b>1.02</b>	1.58	<b>1.14</b>	<b>0.04</b>	0.18
Thalamus	12.90	16.22	5.98	<b>0.77</b>	6.06	<b>0.93</b>	<b>0.08</b>	0.19
Cerebral WM	496.60	403.70	<b>0.88</b>	1.98	<b>0.87</b>	1.91	<b>0.00</b>	0.07

## Experiment 8: Travelling Human Phantom (THP) dataset

The THP data was collected to assess the reliability and robustness of automated algorithms across scans from different centers with different protocols (Magnotta et al., 2012). The dataset includes scans from 5 healthy subjects travelling to 8 different medical centers in the USA. All scans were acquired within a period of 30 days, so that atrophy of the structures due to normal aging is negligible. Each of the 8 imaging centers used MRI scanners manufactured by different vendors, different gradient specifications, different number of channels in the head coil etc. Ideally, the coefficient of variation of volume estimates across the sites should be zero; the lower the estimate, the more reliable and robust is the segmentation algorithm. A detailed explanation of the experimental setup is provided in (Magnotta et al., 2012). Overall, the dataset is challenging for segmentation because it is very heterogeneous with strong variation of data quality across sites, where scans from some sites exhibit strong motion artifacts.

We compared QuickNAT with FreeSurfer and reported the results in Supplementary Table 13. QuickNAT showed more robustness for structures Hippocampus, Putamen, Pallidum and Thalamus, while FreeSurfer is better in Lateral ventricles, Amygdala, Caudate and cerebral WM. All in all, QuickNAT portrayed similar robustness properties like FreeSurfer for this challenging experiment.

Supplementary Table 13: Coefficient of variation (CV) in volume estimation for the 8 structures for each subject, using QuickNAT (QN) and FreeSurfer (FS). Also, RMS CV per structures for all the subjects is presented.

Structures	Subject ID with CV										RMS CV	
	1		2		3		4		5		FS	QN
	FS	QN	FS	QN	FS	QN	FS	QN	FS	QN		
<b>Hippocampus</b>	8.49	4.66	1.41	1.09	2.39	2.18	3.57	1.19	2.69	4.06	4.47	<b>3.02</b>
<b>Lateral Ventricles</b>	8.28	14.8	5.25	8.43	2.37	6.32	2.85	6.62	12.9	15.1	<b>7.45</b>	10.9
<b>Amygdala</b>	4.10	10.4	2.25	5.08	5.33	4.98	2.16	2.99	5.58	5.31	<b>4.15</b>	6.29
<b>Putamen</b>	9.36	5.76	5.66	1.89	5.83	1.30	5.18	1.80	4.29	5.08	6.31	<b>3.63</b>
<b>Pallidum</b>	9.34	5.26	7.59	1.49	9.05	1.59	7.99	1.22	5.27	3.85	7.98	<b>3.12</b>
<b>Caudate</b>	5.12	15.3	2.83	5.72	3.13	1.47	2.45	4.27	3.01	6.75	<b>3.44</b>	8.18
<b>Thalamus</b>	2.74	1.43	4.21	1.11	2.70	2.55	2.42	2.36	5.33	3.49	3.65	<b>2.35</b>
<b>Cerebral WM</b>	3.09	3.43	1.64	3.45	2.59	4.80	2.20	3.79	4.14	4.28	<b>2.86</b>	3.99



## References

- Asman, A.J., Landman, B.A., 2012. Formulating spatially varying performance in the statistical fusion framework. *IEEE Trans. Med. Imaging* 31, 1326–1336.
- Avants, B.B., Tustison, N.J., Song, G., Cook, P.A., Klein, A., Gee, J.C., 2011. A reproducible evaluation of ANTs similarity metric performance in brain image registration. *Neuroimage* 54, 2033–2044.
- Bartsch, T., Wulff, P., 2015. *The hippocampus in aging and disease: from plasticity to vulnerability*. Elsevier.
- Boccardi, M., Bocchetta, M., Morency, F.C., Collins, D.L., Nishikawa, M., Ganzola, R., Grothe, M.J., Wolf, D., Redolfi, A., Pievani, M., 2015. Training labels for hippocampal segmentation based on the EADC-ADNI harmonized hippocampal protocol. *Alzheimers Dement.* 11, 175–183.
- Jack, C.R., Bernstein, M.A., Fox, N.C., Thompson, P., Alexander, G., Harvey, D., Borowski, B., Britson, P.J., L Whitwell, J., Ward, C., 2008. The Alzheimer’s disease neuroimaging initiative (ADNI): MRI methods. *J. Magn. Reson. Imaging* 27, 685–691.
- Jenkinson, M., Beckmann, C.F., Behrens, T.E., Woolrich, M.W., Smith, S.M., 2012. Fsl. *Neuroimage* 62, 782–790.
- Kempton, M.J., Underwood, T.S., Brunton, S., Stylios, F., Schmechtig, A., Ettinger, U., Smith, M.S., Lovestone, S., Crum, W.R., Frangou, S., 2011. A comprehensive testing protocol for MRI neuroanatomical segmentation techniques: evaluation of a novel lateral ventricle segmentation method. *Neuroimage* 58, 1051–1059.
- Kennedy, D.N., Haselgrove, C., Hodge, S.M., Rane, P.S., Makris, N., Frazier, J.A., 2012. CANDIShare: a resource for pediatric neuroimaging data. Springer.
- Landman, B., Warfield, S., 2012. MICCAI 2012 workshop on multi-atlas labeling, in: *Medical Image Computing and Computer Assisted Intervention Conference*.
- Maclaren, J., Han, Z., Vos, S.B., Fischbein, N., Bammer, R., 2014. Reliability of brain volume measurements: A test-retest dataset. *Sci. Data* 1, 140037.
- Magnotta, V.A., Matsui, J.T., Liu, D., Johnson, H.J., Long, J.D., Bolster Jr, B.D., Mueller, B.A., Lim, K., Mori, S., Helmer, K.G., 2012. Multicenter reliability of diffusion tensor imaging. *Brain Connect.* 2, 345–355.
- Marcus, D.S., Wang, T.H., Parker, J., Csernansky, J.G., Morris, J.C., Buckner, R.L., 2007. Open Access Series of Imaging Studies (OASIS): cross-sectional MRI data in young, middle aged, nondemented, and demented older adults. *J. Cogn. Neurosci.* 19, 1498–1507.
- Patenaude, B., Smith, S.M., Kennedy, D.N., Jenkinson, M., 2011. A Bayesian model of shape and appearance for subcortical brain segmentation. *Neuroimage* 56, 907–922.
- Wachinger, C., Reuter, M., Klein, T., 2017. DeepNAT: Deep convolutional neural network for segmenting neuroanatomy. *NeuroImage*.
- Wang, H., Yushkevich, P.A., 2013. Multi-atlas segmentation with joint label fusion and corrective learning—an open source implementation. *Front. Neuroinformatics* 7.